

Exploring hidden priors when interpreting gravitational wave and electromagnetic probes of the nuclear equation of state

Atul Kedia ^{1,2} Richard O’Shaughnessy ¹ Leslie Wade ³ and Anjali Yelikar ¹

¹*Center for Computational Relativity and Gravitation, Rochester Institute of Technology, Rochester, New York 14623, USA*

²*Department of Physics, North Carolina State University, Raleigh, North Carolina 27695, USA*

³*Department of Physics, Kenyon College, Gambier, Ohio 43022, USA*

(Dated: March 3, 2025)

The wide range of sub- and super-nuclear densities achieved in neutron stars makes them ideal probes of dense nuclear behavior in the form of the nuclear equation of state (EoS). Studying neutron stars both in isolation and in highly dynamic events, many recent observations, most famously the gravitational wave and electromagnetic signals associated with the BNS merger GW170817/AT2017gfo, have provided suggestive insight into these highest nuclear densities. Measurements of galactic neutron star masses and radii from NICER and other radio and X-ray measurements provide critical complementary perspectives, bounding other features of the EoS. Though nominally congruent, in this paper we highlight many underappreciated “hidden” priors embedded in joint analysis of these many messengers, and their systematic impact on joint EoS inference. In this work, we perform a careful step-by-step Bayesian inference using a simple low-dimensional parametric EoS model, incrementally adding information from galactic pulsars, gravitational wave sources, and more speculative constraints involving kilonovae and the neutron star maximum mass. At each stage, we carefully discuss the marginal likelihood, explaining how hidden priors impact conclusions. Conversely, we also quantify how much information these measurements have, arguing that many if not most have minimal impact relative to the explicit and hidden prior assumptions. Specifically, we find two features dominate our inference: on the one hand, the choice of EoS parameterization, and on the other the astrophysical priors associated with interpreting events, particularly the multimessenger source GW170817. Spectral parameterizations have been shown to cause large differences in the predicted EoS based on if causality is applied in the framework or not, and applying causality predicts a strong phase-transition-like feature at $\sim 10^{14.5}$ g cm⁻³. In an appendix, we outline a simple semianalytic projection suitable for assessing the measurability of the EoS with ensembles of present and future detections.

I. INTRODUCTION

Neutron star observations, made over the last decades have provided a critical perspective into matter at high densities, complementing rapid theoretical and experimental progress [1–32]. High-precision pulsar observations have provided evidence for a wide range of neutron star masses, constraining the neutron star maximum mass from below [33]. X-ray measurements of neutron star radii have provided additional constraints [32, 34–36]. Recently, the NICER mission has enabled unique neutron star periodic profile monitoring, enabling simultaneous mass and radius constraints on two neutron stars [37–51]. Observations of merging neutron stars have also provided several signatures which potentially limit the nuclear equation of state (EoS). Gravitational wave measurements of GW170817 limit the effective inspiral tidal deformability [3, 12, 14, 24, 52–54]. Simultaneous electromagnetic observations also provide suggestive hints into neutron star compactness, deduced from the presence and energetics of gamma-ray [55] and kilonova [28, 56, 57] emission [3, 12–14, 22, 58–61]. While the origin of quasi-periodic oscillations remain unclear, if these can be attributed to neutron stars, then additional constraints can be formulated [62].

The different approaches largely suggest a comparable neutron star radius (see, e.g., [32] and references therein), as deduced by many groups employing similar Bayesian methods from various independent observational sources and techniques (see Ref. [63] for a review of Bayesian statistics for astrophysical observations). However, the individual underlying inferences involve many often subtle steps which disguise

their implicit and explicit priors, particularly when combining very heterogeneous sources of external information. Unsurprisingly and closely related, looking more closely at individual measurements and their systematics suggests tension between these different observational approaches to the EoS. For example, several studies have pointed out that the amount and nature of material ejected from a merger like GW170817 is inconsistent with the matter needed to reproduce the details of the kilonova emission [64–68]. Conversely, several investigations have wholeheartedly embraced combining all available measurements to produce overall estimates, despite the incremental impact most of these measurements have on overall inferences, owing to large statistical measurement errors (let alone poorly understood systematics); see, e.g., the discussion in [28]. Finally, as highlighted by previous work [32, 69–71], the relative impact of all measurements derives strongly from their explicit prior assumptions, both on the small and large scale. For example, compared to theoretically well-motivated priors [72, 73], adopting an extremely conservative phenomenological approach with much wider priors enables individual measurements to strongly rule out individual realizations (e.g., [74]). Conversely, a too-tightly-parameterized approach could conceivably miss subtle degeneracies associated with putative phase transitions; see, e.g., [75] and references therein.

In this work, we revisit how to combine several different constraints on the nuclear EoS, including explicit and implicit theoretical or astrophysical priors. We demonstrate these inferences rely on rarely discussed and of necessity strong assumptions about the neutron star population. We argue these

often inconsistently-applied prior factors have a substantial effect and may cause analyses to inadvertently rule out a priori consistent EoS models. Conversely, we demonstrate that most extant measurements are largely consistent, with modest tension with each other and our priors even for our most extreme scenarios.

Unlike many recent studies which rely on increasingly complex models for the nuclear EoS, to preserve our emphasis on the observational ingredients and priors we employ an extremely simple low-dimensional model for the nuclear EoS:

two conventional spectral representations [76–78] based on approximating a functional versus (log) pressure with a Taylor series. These low-dimensional smooth approximations are known to have limited flexibility compared with more expressive infinite-dimensional nonparametric models like Gaussian processes [5, 21, 79]. However, these models are more than sufficient to express contemporary observational uncertainties, helping us indicate avenues where systematics may play an important role. Other studies have thoroughly explored more flexible approaches including multiple phase transitions; see, e.g., [74] and references therein.

This paper is organized as follows. In Section II we review our phenomenological spectral approach to the nuclear equation of state; pertinent observations of neutron stars; our specific implementation of hierarchical Bayesian inference for the nuclear equation of state; and our specific procedure and priors for each class of measurement. For galactic neutron stars we employ radio observations of heavy neutron stars PSR-J0348 [80] and PSR-J1641 [81, 82], NICER X-ray pulse profiling for PSR-J0030, PSR-J0740, and X-ray spectra and distance analyzed for HESS J1731 [83] which retains the possibility of consisting of strange quark matter, however for this study we assume it to be nucleonic. For gravitational wave sources, we employ only GW170817. In Section III we provide inferences for the nuclear EoS using galactic pulsars and nuclear symmetry energy; update that inference using information from GW170817, and then reassess those results by incorporating more indirect interpretations of observations, including limits on the NS maximum mass. Finally, we present our concluding remarks in Sec. IV.

II. METHODS

A. Nuclear equation of state phenomenology

Following previous investigations, we characterise the nuclear equation of state with a low-dimensional phenomenological model. Rather than employ a sophisticated but high-dimensional phenomenological approach based on microphysics-motivated calculations with many tunable parameters such as relativistic mean field theory [84–91], for simplicity and lacking observationally-driven necessity, we adopt two distinct analytic representations.

In this work we principally employ a specific and widely-used spectral parameterization [76], referred to as the Γ -spectral parameterization from here onwards, in which the natural log of the zero-temperature adiabatic index $\Gamma =$

$d \ln p / d \ln n$ is expressed as a power series in $\log p$:

$$\ln \Gamma = \sum_k \gamma_k (\ln p / p_o)^k \quad (1)$$

For this model, we adopt a uniform prior in its hyperparameters, with limits consistent with previous studies [2, 92]. Though we do not explicitly enforce other customary constraints (e.g., on the adiabatic index), our TOV solver requires EoS that are nearly causal, so our calculations de facto reject highly unphysical samples as implausible. To illustrate the impact of model and prior systematics, we also employ another spectral formulation, referred to as Υ -spectral from here onwards (though denoted the “improved causal spectral” formulation in Ref. [78]), designed to ensure smooth transition from the fixed low density piece to the fit higher density part and to ensure causality all throughout. In particular we use the pressure based formulation described in [78], where the spectral expansion is constructed for the sound speed dependent parameter $\Upsilon(p)$ defined as

$$\Upsilon(p) = \frac{c^2 - v^2(p)}{v^2(p)} \quad (2)$$

for which the spectral expansion is

$$\Upsilon(p) = \exp \left[\sum_{k=0}^{\infty} \lambda_k \left(\log \left(\frac{p}{p_0} \right) \right)^k \right]. \quad (3)$$

This decomposition is very similar to the previous causal- Γ -spectral representation [77] with the only difference being that the zeroth coefficient, λ_0 , is predetermined. Here λ_0 is fixed such that sound speed continuity is ensured at the matching point, p_0 , between the low density and high density pieces

$$\lambda_0 = \log \left(\frac{c^2 - v_0^2}{v_0^2} \right) \quad (4)$$

We restrict our analyses to the first four independent parameter in this decomposition, $k = 1, 2, 3, 4$, in order to capture systematic features of the EoSs while keeping the exploration manageable. We choose a uniform prior for these four spectral parameters, over $\lambda_1 \in [-3, 3.2]$, $\lambda_2 \in [-4, 2]$, $\lambda_3 \in [-0.2, 0.8]$, and $\lambda_4 \in [-0.05, 0.02]$, where these ranges of each parameter are motivated by covering existing EOS as well as the Γ -spectral posterior for GW170817 [93]. Figure 1 shows our implied prior on $p(\rho)$ and nonrotating neutron star gravitational mass and radius. We use these two parametric approaches to qualitatively assess the kinds of systematic uncertainty exhibited among some of the commonly used parameterizations, such as piecewise polytropic [94], dynamical-piecewise polytropic [92, 95], and similar spectral methods [76–78] which adopt different basis functions or parameters [96].

We follow previous work that employs Gaussian quadrature to evaluate the energy-density at given pressure on the `1alsuite` implementation [2, 92]. We adopt a fixed low-density equation of state with the first four terms in the expansion determining the EoS. This parameterization has been

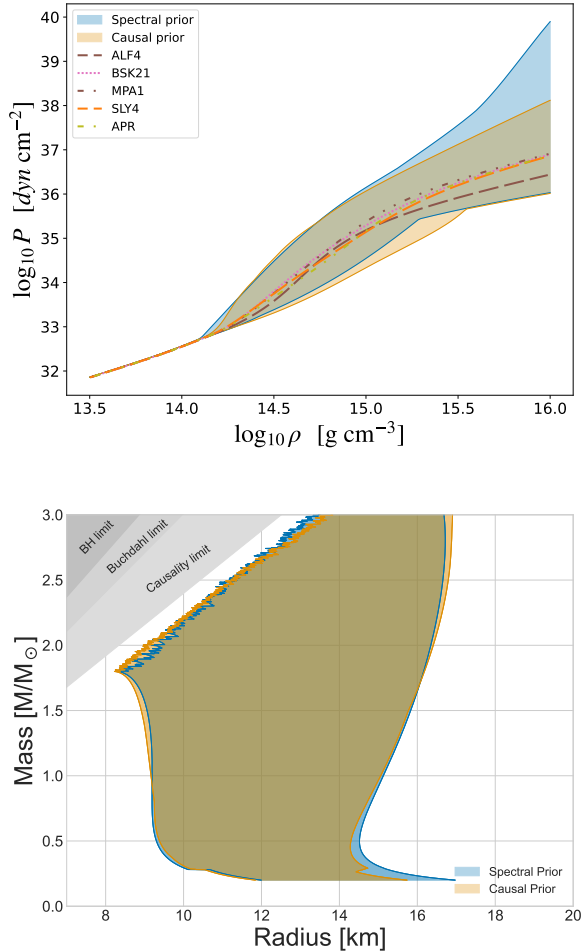


FIG. 1. **Priors** Pressure p versus energy density ρ for cold nuclear matter prior utilized. The shaded region shows the 100% credible interval implied by our fiducial prior on the Γ -spectral model (blue) and Υ -spectral model (orange). Also shown are several fiducial equations of state in dashed and dotted curves, for reference.

Top panel: Pressure-Density priors for the causal and regular spectral representations along with five fiducial EoSs. The interval shown encompasses all draws from our prior (here, shown for 10^4 samples). Bottom panel: Mass-Radius prior range for the EoSs in the above range. The grey shaded regions indicate various constraints on single-stable NS; ‘BH limit’ is where the Schwarzschild radius is larger than the NS radius, ‘Buchdahl limit’ is the range where an NS would need infinite pressure [97], and ‘Causality limit’ is obtained by finding the maximally compact (M/R) solution for Mass-Radius in the limiting physical range of pressure-density [98].

previously constrained by comparison of its input GW170817 [2] and NICER measurements [37, 45]. For all EoSs, we solve the Tolman-Oppenheimer-Volkoff (TOV) equation [99, 100] for nonrotating neutron star structure in hydrostatic equilibrium using RePrimAnd [101, 102] to find one-parameter families of gravitational mass M , radius R , and tidal deformability Λ . The output for an equation of state α is characterized by a one-parameter family $R_\alpha(s), M_\alpha(s)$, where s is a fiducial

parameter characterizing our dimensionless prior. For simplicity, in this work we adopt the pseudo-enthalpy h , and only investigate the lowest stable branch of solutions.

What is a measurement of an equation of state?

Bayesian inference frameworks provide a likelihood and hence (with a prior) probability for each equation of state function. We can therefore interpret observations as providing information about a credible interval on the space of functions: for example, deducing a volume of EoS which contain 90% of all (joint) posterior probability. Figure 1 shows our 100 percentile prior EoS distribution. This interpretation, however, conflicts with the customary approach to rendering and reporting conclusions about the EoS, which are presented as *marginal distributions for (uncorrelated) point measurements*: for example, the distribution of pressure at a given density, or the radius of NS of a fiducial mass. As highlighted in previous work [5], the superposition of point measurements neglects important information including correlations between different densities (for $p(\rho)$) or masses (for $R(M)$). As a concrete example for any two densities ρ_i , the posterior pressures $\ln p(\rho_1), \ln p(\rho_2)$ will be correlated by measurements, above and beyond any correlations introduced by our prior. Nonetheless, in this work to simplify comparison with previously-reported results, except for Figure 1 we render our conclusions using this point-measurement approach. Thus for example a confidence interval on $p(\rho)$ follows by taking all weighted EoS realizations $(p_k(\rho), w_k)$ and, for each reference density ρ_i , constructing a confidence interval for $p(\rho_i)$ using the weighted sample at that density. Similarly but not identical are confidence intervals on $\rho(p)$, constructed similarly but using the inverse relationship.

The conclusions about the EOS posterior described in the preceding paragraph assume only a prior on the functional space of EoS. However, many discussions of the NS mass-radius distribution adopt priors *along* the family of stable NS by, for example, adopting a prior on the NS central density; see, e.g., [45, 74, 103]. As discussed below, these analyses are in effect adopting a prior on the NS mass distribution. As a result, in order to replicate their results, we must present our results in a comparable fashion. Specifically, rather than construct a 90% credible interval for the NS radius at each fixed mass, we must instead construct a two-dimensional marginal distribution in both mass and radius. This two-dimensional posterior distribution will explicitly depend on the choice of NS mass distribution (or equivalently NS central density distribution).

B. Neutron star population models

Deducing the equation of state from observations of neutron star properties always requires some model for the neutron star population: empirical observables limit but do not uniquely determine the neutron star mass, spin, radius, and tidal deformability. In this work, unless otherwise noted, we

will assume the isolated (and binary) neutron star population is uniformly distributed in gravitational mass m between fixed, EoS-independent limits $m \in [m_{min}, m_{max}]$. We specifically adopt $m_{min} = 0.4 M_{\odot}$ and $m_{max} = 2.1 M_{\odot}$, with the lower and upper mass limits chosen because of the collection of NSs we will use to constrain the nuclear EoS. Similarly, unless otherwise noted, we will assume the (aligned component) of neutron star spin is distributed isotropically in a sphere and uniformly in magnitude, with a maximum dimensionless value $a = S^2/m < 0.05$. This fiducial population closely resembles the prior assumptions used when inferring the nature of low-mass gravitational wave sources. We emphasize that our prior represents our assumptions about the *astrophysical distribution* of neutron stars *as realized in nature*, which need not reach the maximum mass allowed by the nuclear equation of state.

For context, other groups have adopted a wide range of different implicit or explicit priors for the neutron star mass distribution. For example, some adopt priors on the neutron star central density, not the neutron star mass (e.g., a quadratic prior [45, 74] or a log-uniform prior [103] between the maximum central density and some reference density). Alternatively, even within the context of nominally uniform mass distributions, others [104] have specifically assumed $p(m|\mathcal{Y})$ is uniform between a fixed minimum mass and the EoS-dependent maximum mass $M_{max}(\mathcal{Y})$, where \mathcal{Y} here and henceforth denotes the EoS or its parameterization. In other words, this model asserts all NSs that can exist under an EoS do exist. In terms of the unit step function $\Theta_I(x) = 1$ for $x \in I$ (I being the interval) and 0 otherwise, their one- and two-dimensional priors are $p(m) = \Theta_I(m)/|I|$ and $p(m_1, m_2) = 2\Theta_I(m_1)\Theta_I(m_2)\Theta(m_1 - m_2)/|I|^2$, where $I = [m_{min}, M_{max}(\mathcal{Y})]$ is the interval between m_{min} and the EoS-dependent maximum mass. Compared to our fiducial approach, both of these aggressive population models introduce EoS-dependent normalization factors, which weakly penalizes models with large $M_{max}(\mathcal{Y})$ for single observations and strongly penalize them for many observations. Additionally, these aggressive population models should be strongly constrained by the absence of massive neutron stars; see, e.g., Alsing et al. [105, 106] and references therein. For broader context regarding prior choices, Wysocki et al. [93] demonstrated that, if not known a priori, the neutron star mass distribution and EoS must be jointly inferred, to avoid biasing the deduced EoS. In the main text and in appendices we will briefly discuss how alternative mass priors can impact our results.

Several sources of external information provide good reason to adopt alternative informed priors. For example, several authors have proposed adopting comparable masses for binary neutron stars, motivated by galactic observations and conventional field formation scenarios which strongly favor nearly equal masses [107–111]. Similar arguments have been employed to rule out large or preferentially negatively-oriented spins [112]. (Of course, the limited statistics available from the GW census are consistent with a much broader mass ratio distribution [79, 113] and provide minimal constraints on plausible NS spin orientations; additionally, non-merging galactic BNS binaries have a much broader mass ratio dis-

tribution [114].) At the other extreme, because the kilonova AT2017gfo associated with GW170817 suggests very massive dynamical ejecta and since most predictions for this ejecta are suppressed for $q \simeq 1$, others have suggested favoring asymmetric masses where the dynamical ejecta isn't suppressed [115, 116]. On similar grounds based on AT2017gfo, others have demonstrated that a strongly-spinning secondary neutron star (m_2) will produce substantially enhanced ejecta, as its outer layers are less bound [117, 118]. Strongly spinning NS mergers can occur for example if the secondary does not have time to spin down, due to fortuitous NS kicks [119] or Kozai-Lidov effects in hierarchical triples [120]. (Such a rapid formation scenario isn't consistent with the large geometric offset for AT2017gfo but could occur in general; as noted in [120, 121] this rapid formation scenario would reconcile NS merger formation with r-process-enriched but metal-poor stars.) Particularly given the systematics associated with contemporary ejecta calculations, an exhaustive quantitative investigation of these additional speculative sources of prior information merits its own dedicated study.

Motivated by the discussion in the preceding paragraphs, we will analyze GW170817 with combinations of several alternative priors. To focus on high mass ratios only, we will perform some analyses with a mass ratio distribution $p(q)$ for AT2017gfo that is consistent with a uniform distribution of component masses but excludes $m_2/m_1 > 0.6$. (At GW170817's source-frame chirp mass $\mathcal{M}_c = 1.186 M_{\odot}$, this constraint requires more extreme choices for source-frame primary and secondary mass: $m_2 < 1.062 M_{\odot}$ and $m_1 > 1.77 M_{\odot}$.) Conversely, when requiring GW170817's mass ratio prior distribution be constrained to the range expected for GW-detected BNS sources derived from the galactic population, we require $m_2/m_1 > 0.9$ [107]. To allow for extreme spins, we consider an isotropic uniform spin magnitude prior which extends to 0.4. To strongly disfavor extreme spin-orbit misalignment, we consider $\chi_{i,z} > 0$. Operationally, all of these astrophysical prior choices can be implemented as alternative options for the upper and lower bounds adopted for $q, \chi_{i,z}$, when analyzing GW170817 with a nonprecessing GW model.

C. Neutron star mass-radius constraints

NICER observations of periodic X-ray emission on millisecond pulsars provides information about their masses and radii. Though their data product is reported as a weighted posterior distribution, we find these results can be well approximated by a simple Gaussian distribution, as illustrated in Figure 2 for the pulsar PSR-J0030 (red). In Appendix A we describe the best-fitting gaussian to each NICER (alongside HESS) observation, and the specific method we used to deduce its parameters. In terms of this Gaussian likelihood $L(M, R)$, we can evaluate the marginal likelihood for each

equation of state α according to [63, 122, 123]

$$\begin{aligned} Z(\alpha) &= \int \left[\int \mathcal{L}(M, R) \delta(R - R_\alpha(s)) \right. \\ &\quad \left. \delta(M - M_\alpha(s)) dM dR \right] p(s) ds \\ &= \int \mathcal{L}(M(s), R_\alpha(M(s))) p(s) \frac{dM}{dM_\alpha/ds} \\ &= \mathcal{F} \int \mathcal{L}(M(s), R_\alpha(M(s))) dM \end{aligned} \quad (5)$$

$$(6)$$

where s is a fiducial parameter characterizing our dimensionless prior along each one-parameter family of each EoS; $p(s)$ is a prior along that one-parameter family; and in the last line we've chosen $p(s)$ to be compatible with our uniform prior over the neutron star mass, with \mathcal{F} the appropriate normalization constant in mass space: $\mathcal{F} = 1/(m_{max} - m_{min})$. For simplicity, in this work we adopt the gravitational mass M as our fiducial prior (i.e., so the denominator $(dM_\alpha/ds)/p(s)$ is constant), while recognizing the utility of other global choices like the pseudo-enthalpy. This choice of prior along each family strongly downweights contributions to the evidence near turning points in the mass-radius plane at the high and low mass ends of the curve (i.e., $dM/dR \simeq 0$). That said, our choice of prior enables us to use the same functional form for all equations of state, independent of their maximum mass.

For comparison, other priors will inherit different prior mass distributions from their prior on the assumed parameterization s . If instead one follows Ref. [74] and chooses s to be the central density and $p(\rho_c)$ to be some prior on that central density, then the implied mass distribution is proportional to $p(\rho_c)/dM/d\rho_c$. Equivalently, the cumulative distribution function for any individual equation of state satisfies $P(< \rho_c) = P(< M(\rho_c))$, for simplicity assuming a single-branched relationship between mass and central density. The specific prior adopted in [74] very strongly favors massive binaries, where dR/dM is large.

Most neutron star mass measurements provide information only about the empirical pulsar star mass distribution, rather than any direct insight into the nuclear equation of state. However, a few very massive pulsars' existence provides useful insight into the neutron star maximum mass, bounding it from below: J0740 [124, 125], with pulsar mass consistent with a Gaussian with mean and standard deviation $2.14 M_\odot$ and $0.1 M_\odot$; J0348+0432 [126], with pulsar mass $2.01 M_\odot \pm 0.04 M_\odot$; and J1614 [127], with pulsar mass $1.908 M_\odot \pm 0.016 M_\odot$. We follow [28] to express the likelihood of an EoS consistent with these observations as the product of standard normal distributions:

$$\mathcal{L}_\alpha = \prod_k \Phi \left(\frac{M_{max,\alpha} - M_{*,k}}{\sigma_{*,k}} \right) \quad (7)$$

where $\Phi(z)$ is the cumulative distribution of the standard normal distribution for each maximum mass measurement and are shown in Fig. 2 as horizontal bands.

As a demo, Figure 2 shows the Mass-Radius curves for sample nuclear EoSs, AP4, MPA1, BSK21, SLY4, and ALF4,

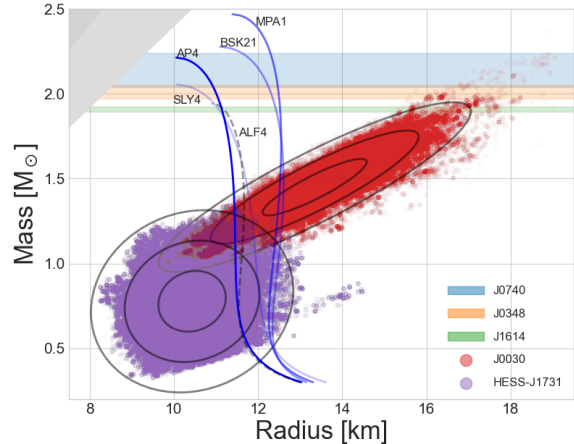


FIG. 2. **Methodology** Mass-Radius likelihoods evaluated for sample cold nuclear EoSs. The pulsar constraints used for the likelihoods are shown in the background in various colors. Darker colors of the M-R curves indicate higher log likelihood for each EoS. The EoS with the lowest likelihood is represented with a dashed curve. The red and purple patches are the posterior samples from NICER pulse profile of PSR-J0030 and the HESS-J1731 respectively. The horizontal color bands are mass constraints of J0740, J0348, J1614.

plotted over the NICER constraints posteriors by their likelihoods. The EoSs are selected to demonstrate how inference is conducted in this work via the multiple different channels informing about consistency with the particular measurement. The darker shaded M-R curves of the various EoSs (MPA1, and AP4 in this example) indicates greater relative likelihood of those EoSs in comparison to the lighter colored EoSs (SLY4 and BSK21). Note ALF4, which is hardly visible, is so due to it not supporting the maximum mass observations. In our likelihood evaluations for grids of EoSs we employ this method for applying Mass-Radius constraints.

D. Gravitational wave observations

Gravitational wave observations of GW170817 constrain the binary masses m_i and tidal deformabilities Λ_i for each component of the binary [1–3, 128]. Specifically, the presence of matter at leading order impacts the binary's inspiral, through each components' dimensionless tidal deformability parameter $\Lambda = (2/3)k_2(c^2R/GM)^5$ [129], where k_2 is the $l=2$ Love number, M is the mass, and R is the radius. The leading order contribution to the phase evolution of an GW inspiral is given by the weighted combination of Λ terms

$$\tilde{\Lambda} = \frac{16}{13} \frac{(m_1 + 12m_2)m_1^4\Lambda_1 + (m_2 + 12m_1)m_2^4\Lambda_2}{(m_1 + m_2)^5} \quad (8)$$

The impact of tidal effects are included in many conventional approximate phenomenological estimates of outgoing radiation from merging compact binaries. In this work, we will focus on analyses with a contemporary state-of-the-art model,

IMRPhenomPv2_NRTidalv2 [130, 131], which incorporates precession physics but omits higher-order modes. We note other contemporary models like NRHybSur3dq8Tidal [132] and TEOBResumS [133] include these higher-order modes and tidal effects.

Using the marginal likelihood $L(X)$ obtained by interpolating the RIFT marginal likelihoods and the EoS-derived relationship connecting $\Lambda(m|\mathcal{Y})$ to the neutron star gravitational mass m and equation of state model \mathcal{Y} , we compute a marginal evidence

$$\mathcal{E} = \int L(X(x, \mathcal{Y}))p(x)dx \quad (9)$$

where $x = (m_1, m_2, \chi_1, \chi_2)$ are binary parameters omitting tides and X supplements these parameters with the EoS-derived tidal parameters (i.e., $X = (\mathcal{M}_c, \eta, \chi_1, \chi_2, \Lambda(m_1), \Lambda(m_2))$). For simplicity, we also use RIFT to perform this integral [122, 123], using the RIFT marginal likelihood estimator $\hat{L}(X)$ for $L(X)$. These EoS evidence infrastructure has been validated in previous work [123]. We do not employ any customary approximations when evaluating this integral numerically (e.g., that the chirp mass is well known).

While other objects putatively containing matter have been identified via their GW signature (i.e., GW190425 [134], GW200105, and GW200115 [135]), their GW signature also does not meaningfully contain the nature of nuclear matter. For example, the two objects in NSBH binaries have putative matter effects that minimally impact $\tilde{\Lambda}$. Conversely, in GW190425, the large NS masses imply very small tidal deformabilities, but that low-amplitude GW measurement only weakly constraints $\tilde{\Lambda}$. For this reason, we omit further discussion of these three objects.

Phenomenology of Λ , R

To provide a preliminary estimate of the impact of the hidden NS population priors on EoS inference derived from GW170817, we follow Zhao and Lattimer 2018 [136], and adopt simple approximate relationships between tidal deformability and fiducial NS radius $R_{1.4}$. In brief, they argue that to a good approximation $\Lambda \propto (R/M)^6$ (Eq. (13) in Ref. [136]); that therefore $\tilde{\Lambda}$ is to a good approximation proportional to $(R_{1.4}/\mathcal{M}_c)^6$, with a nearly mass-ratio-independent constant (Eq. (15) in Ref. [136]); and therefore for a binary with well-measured chirp mass, the radius of a fiducial NS can be estimated as (evaluated for GW170817)

$$R_{1.4} \simeq 13.4 \text{ km} (\tilde{\Lambda}/800)^{1/6}. \quad (10)$$

E. Additional sources of external information

In the preceding subsections, we have highlighted the essential components for any joint analysis for the nuclear EoS from these astrophysical observations, each with relatively well-understood observational and theoretical systematics. However, other groups have proposed employing other

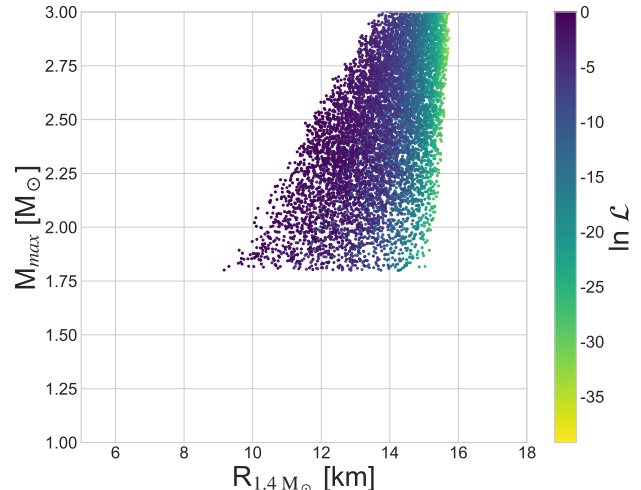


FIG. 3. **Marginal likelihood for symmetry energy**: scatterplot of the symmetry energy likelihood evaluated for many Γ -spectral EoS realizations, versus the corresponding $R_{1.4}, M_{max}$ evaluated for the same EoS realizations. Roughly speaking and within the context of this model family, this symmetry energy constraint favors smaller radii at each fixed M_{max} .

sources of information about the nuclear equation of state to further sharpen their analysis. Below, we summarize three particularly tractable approaches to incorporate specific sources of external information.

The nuclear EoS must be consistent with properties of nuclei [73, 98]. Following [45], one strategy for incorporating information about nuclear-density matter is to require the baryon density n and energy density ρc^2 to be consistent with constraints on the nuclear symmetry energy $S \simeq \rho/n - m_n c^2$, assumed to be known to be normally constrained with a mean of 32 MeV and a standard deviation of 2 MeV at saturation density, assumed to be $2.7 \times 10^{14} \text{ g cm}^{-3}$ [74, 137, 138]. Figure 3 shows the marginal likelihood for different EoS realizations, plotted versus two EoS properties $R_{1.4}$ and M_{max} . The symmetry energy constraint favors smaller radii at each fixed M_{max} .

Based on observations of AT2017gfo, several groups have argued that the observed electromagnetic energetics cannot be consistent with prompt collapse of the remnant to a black hole, using that qualitative constraint to infer an *upper* bound to the NS maximum mass; see, e.g., [54, 55, 139–141] and references therein. Roughly speaking, these arguments suggest $M_{max} < 2.3 M_{\odot}$ [55], extremely close to the mass inferred for J0952-0607 [141].

As noted in Section II B, the observation of AT2017gfo favors large amounts of ejecta. While these large ejecta masses can be accommodated with exceptional NS spins or mass ratios, these outcomes can also be produced with large neutron stars. Using this rationale, some groups have argued that the NS tidal deformability should be bounded below by approximately $\tilde{\Lambda} > 400$ [53]. This proposed constraint on $\tilde{\Lambda}$ has com-

parable qualitative impact on the information obtained from GW170817 as our constraint that $q > 0.9$ and $\chi_{i,z} > 0$, as will be seen in Section III B Figure 7. For brevity, we omit further discussion of this proposal.

A preliminary analysis with the inclusion of a recently measured galactic pulsar J0437 [142] is discussed in Appendix E.

F. Combining multiple measurements

We combine multiple real or synthetic observations by multiplying their likelihoods together, along with a prior $p(\mathcal{Y})$ over the nuclear equation of state parameters \mathcal{Y} (here $\mathcal{Y} = (\lambda_1, \lambda_2, \dots)$ the parameters of spectral representation):

$$\mathcal{L}_{\text{net}}(\mathcal{Y})p(\mathcal{Y}) = \left[\prod_n Z_n(\mathcal{Y}) \right] \left[\prod_k \mathcal{L}_k \right] \left[\prod_g \mathcal{E}_g \right] p(\mathcal{Y}) \quad (11)$$

In this expression, n indexes the neutron star mass radius observations and Z_k is computed according to Eq. (6); k indexes the pulsar mass measurements providing a useful constraint on the maximum neutron star mass, with \mathcal{L}_k computed using one of the factors in Eq. (7); and g indexes the gravitational wave observations, with the GW likelihood computed via Eq. (9). In the equation presented above, for simplicity we have not incorporated two factors superfluous to our study but essential to real analyses of the unknown neutron star populations: survey selection biases and models for the unknown neutron star population. For example, unbiased estimates of the nuclear equation of state require self-consistent estimates of the binary neutron star population [93]. In turn, self-consistent population estimates must correctly account for parameter-dependent selection effects [143, 144].

G. Hyperparameter posterior pipeline: HyperPipe

To generate the posterior distribution from \mathcal{L}_{net} and $p(\mathcal{Y})$ we follow the RIFT iterative inference strategy HyperPipe. Starting with some proposed parameters \mathcal{Y}_α , we evaluate $\mathcal{L}_{\text{net}}(\mathcal{Y}_\alpha) \equiv \mathcal{L}_{\text{net},\alpha}$; build an approximation $\mathcal{L}(\mathcal{Y})$; and use that approximation with an adaptive Monte Carlo integration program to generate both an estimated posterior distribution for \mathcal{Y} as well as a new set of proposed parameters \mathcal{Y}_α' meriting further investigation. This pipeline is able to adaptively explore the space of selected hyperparameters to resolve distinct features in the posterior distribution. The estimate is initiated in a small region of the hyperparameter space (in this case a subsection of the space of $\lambda_1, \lambda_2, \dots$). We refer to the proposed parameter selection, \mathcal{Y}_α , as the *initial grid* of parameters and the resultant physical properties as *initial samples*. Following the first iteration of evaluating likelihoods a posterior is estimated by performing Monte Carlo integration. Following this new parameters are sampled in the regions of the posterior with lower resolution in order to not exclude

important finer details in addition to samples placed in exploratory regions. Following likelihood evaluations for these new points an updated posterior is evaluated by using prior and marginal likelihood information from samples of the previous iteration(s) and the current iteration, hence being better informed. Following this the process is repeated a few times where new sample points are generated and the posterior updated by Monte Carlo integration until the posterior does not deviate between iteration to iteration, resulting in a stable posterior estimate.

For this, we have extended the open-source RIFT inference package to include a general-purpose implementation of this algorithm. Our implementation not only provides a physics-neutral implementation of the RIFT algorithm, but also can interface with generic codes which compute marginal evidence factors appearing in multi-event and multi-messenger inference like Eq. (11). Moreover, though not used here as the pertinent factors are constant in this study, our implementation can include the necessary population-averaged integrals needed to account for a flexible population model and survey selection effects associated each class of measurement (i.e., the full inhomogeneous Poisson likelihood [144] or the rate-marginalized likelihood [143, 145]). Similarly, we can also easily account for multinomial leave-few-out averaged results; for example, to marginalize over including the HESS result or not, the factor \mathcal{E} for the HESS result can be replaced by $\mathcal{E}p + (1 - p)$ and then marginalized over confidence p in that analysis.

H. Diagnostics

As the posterior distribution is directly proportional to the likelihood \mathcal{L}_{net} , we employ several representations of $\ln \mathcal{L}_{\text{net}}$ and its component factors, to characterize the constraining power of each individual observation. As a demonstration, the top panel in Figure 4 shows our marginal log-likelihood $\ln \mathcal{L}$ evaluated using EoS drawn from the full set of marginal likelihood evaluations produced during a hierarchical inference of the EoS, rendered versus $R_{1.4}$, the radius of a fiducial neutron star. In this calculation, the list of equations of state α are drawn from the broad analyses performed in this work. Even more transparently than the two-dimensional approach adopted in Figure 2, this one-dimensional representation allows us to visually illustrate how well each individual measurement constrains one feature of the equation of state. Similarly, the bottom panel in Figure 4 shows our marginal log-likelihood $\ln \mathcal{L}$ versus M_{max} .

These diagnostics allow us to quickly propagate and interpret the effect of different prior choices about the neutron star population. For example, adopting an alternative neutron star mass distribution that is uniform out to $M_{\text{max}}(\alpha)$ instead of a fixed value (such as in this study) shifts log likelihood for each individual likelihood contribution in $\ln \mathcal{L}$ by a factor $-\ln \frac{M_{\text{max}} - m_{\text{min}}}{2.1 M_\odot - m_{\text{min}}}$. Because this systematic factor appears along with every mass-radius measurement, its effects stack as more measurements accumulate, increasingly penalizing configurations with exceptional M_{max} relative to our approach. For

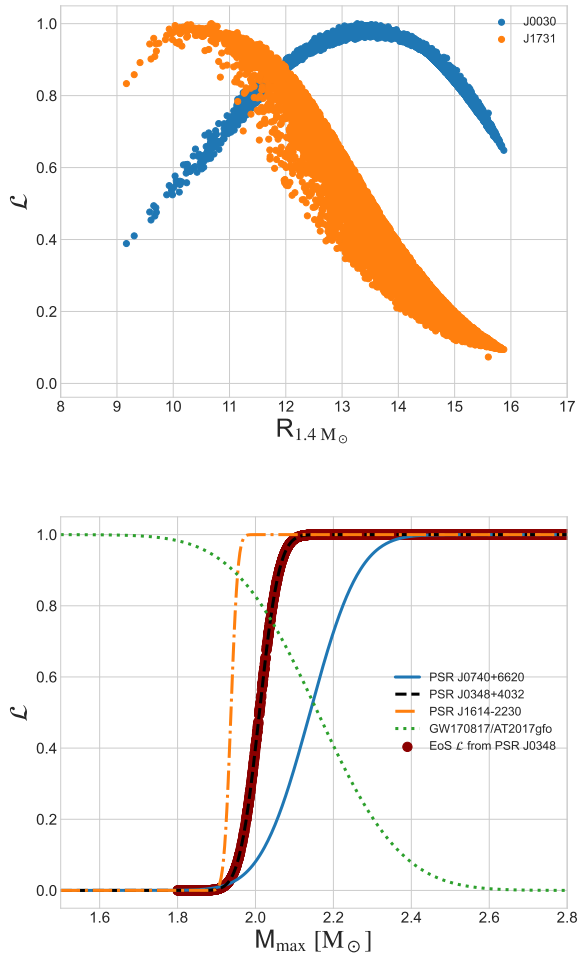


FIG. 4. *Top panel:* Likelihood \mathcal{L} versus $R_{1.4}$ deduced by comparing realizations of the Γ spectral EoS family to the NICER mass-radius constraints of J0030 (blue) and HESS J1731 (orange) *Bottom panel:* Likelihood \mathcal{L} versus M_{\max} . The blue solid, black dashed, and orange dash-dotted lines show Eq. (7), evaluated for each known pulsar mass. The dark-red points show a direct evaluation using realizations of the Γ spectral EoS family to the pulsar J0348, for expediency using `lalsuite` rather than `RePrimAnd` to evaluate M_{\max} for each EoS. The dotted green line shows the hypothesized lower bound on the maximum mass implied by prompt collapse to a black hole; see Section II E for discussion.

expected choices for M_{\max} , however, this factor is small and should have minimal impact on our posteriors.

III. RESULTS

In this section we describe inferences about the EoS, both to compare our methods against previous work and to identify challenges, along with demonstrating the impact of NS population distribution on source properties.

A. Inferences using galactic pulsars

We first reanalyze previously-studied events with our approach, initially using the original spectral parameterizations and priors for the assumed nuclear equation of state. To illustrate how our analysis proceeds using comparable constraints as in [45] (i.e., galactic neutron star observations and the nuclear symmetry energy), the colored scatterplot points in top left panel of Figure 5 show the marginal likelihoods versus the four model hyperparameters (Γ -spectral parameters in this case). In this example, we are employing all the galactic pulsar mass and radius measurements mentioned in Section II C (i.e., mass-radius information for PSR-J0030, and mass measurements for J0740, J0348, J1614), as well as the lower bounds on maximum neutron star mass from observed massive pulsars, as indicated in Figure 2. As described in Section II G, these likelihood evaluations have been identified by `HyperPipe` by conducting an iterative exploration of the model space, in the process recovering the posterior distribution, whose 90% credible intervals and one-dimensional marginal distributions are also shown in the same panel of Figure 5. As expected given how broad and weak our present observational constraints on neutron star radius as illustrated in Figure 2, we find our marginal likelihoods are relatively uniform over a wide range of the parameter space, insofar as EoS compatible with those parameters exist. (Most of our nominally uniform prior volume encompasses incompatible EoS.) Next, the curves in the top-right (bottom) panels express the 90% credible interval of our inferred equation of state in $p(\rho)$ ($M(R)$). Once again, we see that our posterior 90% credible pointwise interval only differs modestly from the full range suggested by our initial assumptions, being narrower at all Mass-Radius estimates. The initial sample space is only indicative of the EoSs taken into consideration at first, as `HyperPipe` selects new points to explore, the posterior is free to go beyond this initial sample limits to attain the best fit. Overall, because our prior assumptions are very well adapted to contemporary theoretical preferences, the new NICER observations add relatively little new additional information over and beyond our original preferences, with one important exception highlighted below.

To investigate the impact of the EoS parameterization (and prior), we also inferred the EoS with the Υ -spectral family. Figure 6 shows a comparable analysis derived using the Υ -spectral parameterization (e.g. Ref. 3), illustrating the inferred relationships between pressure and density, and mass and radius. In this figure we construct $p(\rho)$ posterior distributions using one-dimensional credible intervals at each density, while $M(R)$ is constructed similarly versus M . In sharp contrast to our fiducial analysis with the Γ -spectral parameterization, the Υ -spectral parameterization converges to extreme EoS at low and high density. Close to our matching density with the fixed crust EoS, this Υ -spectral posterior converges to sharp density transitions, consistent with $c_s \simeq 0$. At the densities $\gtrsim 10^{14.5} \text{ g cm}^{-3}$, however, $c_s \rightarrow \infty$. In other words, this alternative parameterization (with broader priors) best fits galactic pulsar observations with strong low-density phase transitions and unexpected high-density behavior, so the

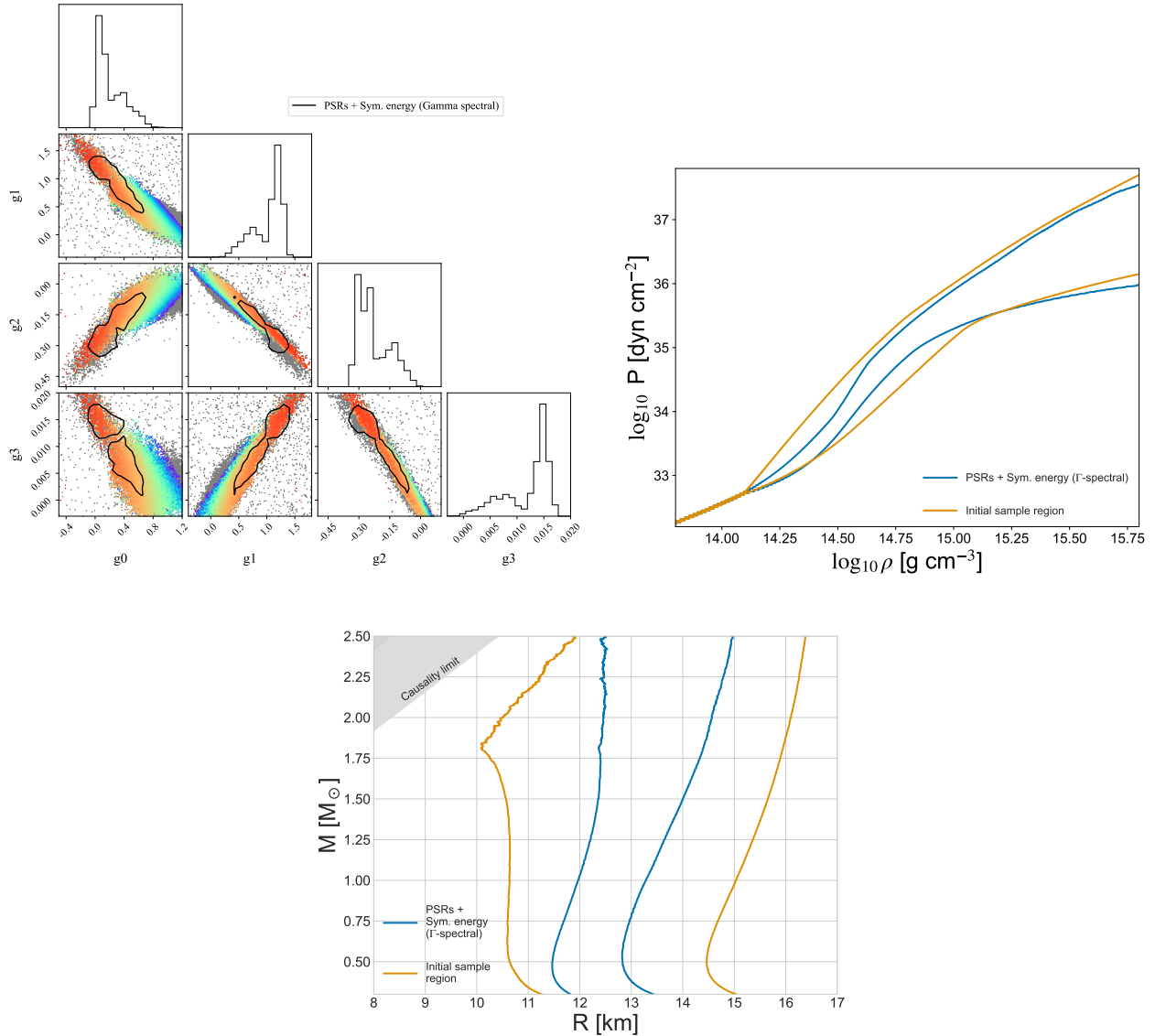


FIG. 5. **EoS inference from galactic pulsars and symmetry energy, Γ -spectral family:** Marginal posterior distribution for the combined inference of observations PSRs J0030, J0348, J0740, J1614, and applying the PREX symmetry energy constraint. *Top-left panel:* Distribution of Γ -spectral hyperparameters. Color scale shows the marginal likelihood, with red indicating the largest values and the solid contour shows the 90% credible interval, while one-dimensional histograms show a one-dimensional marginal distribution. *Top-right panel:* 90% credible interval of pressure versus density, evaluated at each density. *Bottom panel:* 90% credible interval for radius evaluated at each NS mass, rendered as mass versus radius. In the figures in the top-right and bottom the 98% interval of the region covered by the initial samples supplied to HyperPipe is also shown.

$M(R)$ curve aligns more closely with astrophysical results, notably the NICER observation. While the EoS $p(\rho)$ and $c_s(\rho)$ have unexpected behavior, this model family of course produces mass-radius behavior consistent with astrophysical constraints, which are most informative in radius over a narrow mass range.

Considering only the observational marginal likelihood $\ln \mathcal{L}_{\text{net}}$ and disregarding EoS priors, our inferences favor the Υ -spectral family relative to the Γ -spectral EoS. Specifically comparing the largest marginal likelihood $\ln \mathcal{L}_{\text{net}}$ identified in each analysis, we find the Υ -spectral recovers a slightly-larger

peak marginal likelihood, with

$$\frac{\mathcal{L}_{\Upsilon, \text{max}}}{\mathcal{L}_{\Gamma, \text{max}}} \sim 2.39 . \quad (12)$$

Moreover, the best-fitting EoS identified by the Υ -spectral family has qualitative differences from the EoS explored with the Γ -spectral EoS: a regime of EoSs with an early phase-transition followed by a sharp upturn such that $c_s \rightarrow \infty$. We attribute the differences between the two parameterizations' results to their underlying form: given our fiducial hyperparameter priors, the Γ -spectral framework is not sufficiently

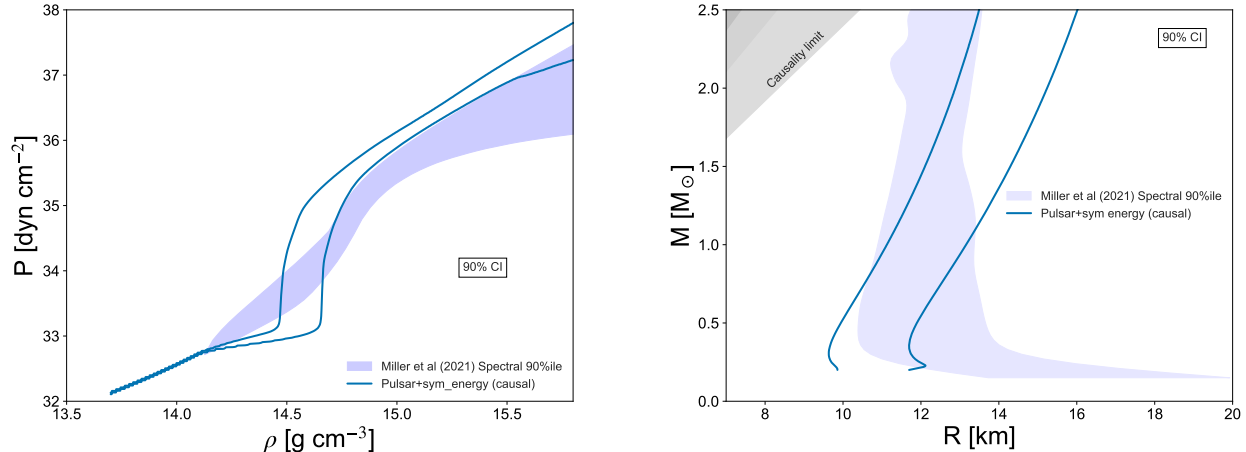


FIG. 6. **Impact of parameterization on EoS inference:** Like Figure 5, but adopting the Υ -spectral EoS, and constraining for only the PSRs J0030, J0348, J0740, J1614 and PREX symmetry energy. We also provide a benchmark analysis with the same PSRs, and symmetry energy, but includes GW constraint and uses Γ -spectral parameterization for these constraints for reference [45].

flexible to produce EoSs with such sharp jumps. Our study corroborates many previous investigations on how different EoS parameterizations, priors, and phase transitions implementations can remain consistent with observations yet correspond to very different underlying conclusions about nuclear physics.

B. Adding information from GW sources

In order to jointly infer the nuclear EOS simultaneously using PSR and GW observations, we need the gravitational wave likelihood $L(X)$ in Eq. (9), to compute the appropriate marginal evidence \mathcal{E} for each EOS. In this section, we first describe our reanalysis of GW170817, with which we construct the necessary marginal likelihood. We then demonstrate, using this phenomenological approach alone and without recourse to detailed EOS modeling, that the posterior for $\tilde{\Lambda}$ depends strongly on the assumed BNS population prior adopted, specifically using three concrete examples motivated in Section II D. We discuss the correlations and features of the GW posterior that cause these prior changes to have the large effect on the $\tilde{\Lambda}$ posterior, and reflect on whether they are robust to other modeling systematics. Finally, using the likelihood provided by this analysis, we perform full-end-to-end EOS inference with the GW and PSR likelihoods together, for the different BNS population prior models discussed above. As anticipated by our simple order-of-magnitude argument using only the posterior for $\tilde{\Lambda}$, we find the BNS population priors have a substantial effect on conclusions about the nuclear EOS.

1. Reanalysis of GW170817 alone

As a benchmark analysis including tidal effects, we analyze open GW data for GW170817 available from GWOSC [146],

using the same PSDs provided with GWTC-1 [147, 148], over a frequency range from 23Hz to 1700Hz [149, 150]. By default, we adopt a low-spin prior $|\chi_i| < 0.05$, with known sky location and source luminosity distance derived from the electromagnetically-identified host galaxy. We do not impose any constraints on the tidal deformability, allowing both Λ_i to take on arbitrary values. Other prior assumptions are customary (e.g., uniform in detector-frame component masses). We include prior information about the alignment between the binary’s angular momentum direction and the line of sight, inferred from late-time radio afterglow observation [151, 152]. For simplicity and without loss of generality we assume both component spins are parallel to the orbital angular momentum direction, primarily to facilitate external constraints on the binary’s orbital inclination. Parameter inference is performed with the most recent RIFT compact binary parameter inference engine [122, 153, 154].

Figure 7 shows our results for the joint posterior in mass, aligned effective inspiral spin χ_{eff} , and tidal deformability $\tilde{\Lambda}$, showing both the posterior (contours) and marginal likelihood (points), obtained using different prior assumptions about the BNS population. All marginal likelihoods accumulated during multiple independent analyses of GW170817, performed with different intrinsic priors but with the same data handling and priors over extrinsic parameters are shown. Some of these prior assumptions by construction limit the range of spins and q allowed, so sharp edges in posteriors associated with the prior constraints are expected and natural. For the fiducial analysis (black), the marginal distributions of mass, mass ratio, spin, and $\tilde{\Lambda}$ are consistent with previously published interpretations using comparable models, settings, and data [1, 2]. For comparison and to highlight the impact of astrophysically plausible prior assumptions on source parameter inferences, this figure also shows analyses in which we require either $q > 0.9$, $\chi_{i,z} > 0$, or both. As the likelihood contains strong correlated features, these constraints impact the posterior dis-

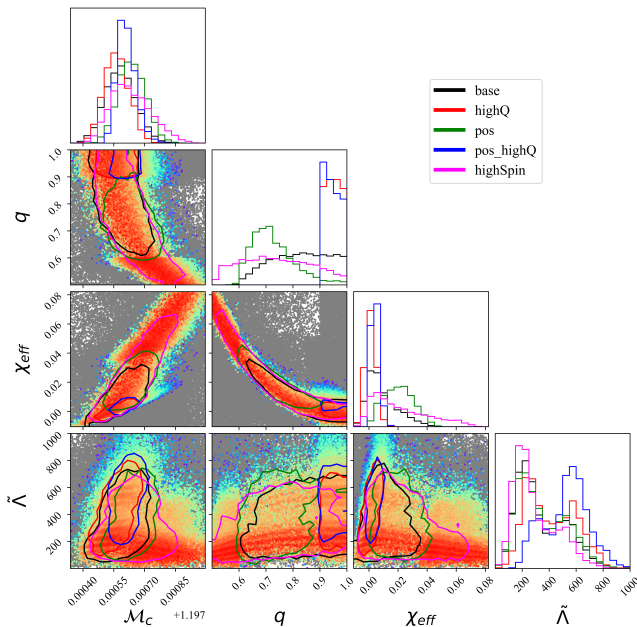


FIG. 7. **GW inference** Benchmark inference of properties of GW170817 using RIFT and IMRPhenomPv2_NRTidalv2. Color scale shows the inferred marginal likelihood, increasing from blue to red over a range of 15 in log-likelihood (with gray indicating values more than 15 below the peak); 2d contours show the 90% credible intervals; and one-dimensional distributions show the one-dimensional marginal posterior distributions. Parameters shown are the detector-frame chirp mass (denoted here by \mathcal{M}_c), mass ratio $q = m_2/m_1$, aligned effective inspiral spin χ_{eff} , and tidal deformability $\tilde{\Lambda}$. Results for our fiducial analysis (in black) shown here are very similar to published results available through GWOSC [1, 2]. Colors indicate results derived using fiducial priors (black); $q > 0.8$ (red); $\chi_{i,z} > 0$ (green); and both (blue). The magenta curve shows results derived with a spin prior extending up to $|\chi_i| = 0.4$.

tribution of tidal deformability $\tilde{\Lambda}$. As seen in the $\tilde{\Lambda} - \chi_{\text{eff}}$ 2-d posterior, when applying only the $q > 0.9$ condition the strong correlation between $\tilde{\Lambda}$ and χ_{eff} requires negative χ_{eff} for small $\tilde{\Lambda}$. As a result, by further requiring that $\chi_i > 0$, we eliminate the possibility that $\tilde{\Lambda}$ can be small (blue). I.e., when applied individually, these two constraints have modest impact. However, when imposed simultaneously, even these modest constraints produce qualitative changes in the inferred tidal deformability.

Figures 7 and 8 also illustrate inferences derived using even more extreme prior assumptions about the pertinent neutron star spin and mass ratio. For example, for the magenta curve provided in Figure 7, the analysis merely allowed for larger possible values of the NS maximum spin. Relaxing the upper limit on χ_i allows a lower mass for m_2 to remain consistent with the data [2], while increasing χ_i only incrementally. Though this single changed assumption allows for more extreme masses, in isolation this one relaxed assumption doesn't change our qualitative interpretation; notably, the distribution of $\tilde{\Lambda}$ is nearly unchanged. By contrast, Figure 8 shows inferences derived assuming $m_2/m_1 < 0.6$, both adopting fiducial

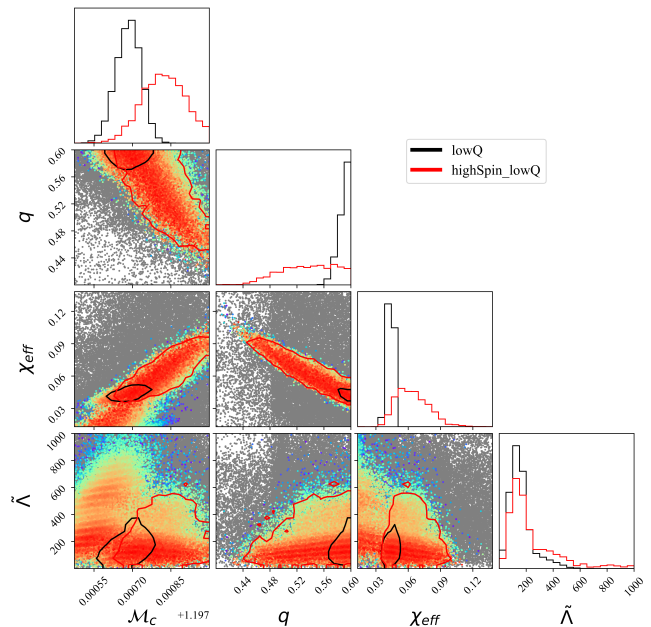


FIG. 8. **GW inference assuming high mass ratio** A reanalysis of GW170817 using RIFT and IMRPhenomPv2_NRTidalv2 while requiring $m_2/m_1 < 0.6$. As in Figure 7, the color scale shows the marginal likelihood and lines show one or two-dimensional marginal distributions. The solid black line adopts the fiducial spin prior $|\chi_i| < 0.05$; the red line adopts a prior of similar form but allows much larger component spins $|\chi_i| < 0.4$. Unlike the results presented in Figure 7, these investigations use a uniform prior on $\chi_{i,z}$, rather than the “z prior”, to ensure comprehensive coverage. Due to strong correlations between spin and mass ratio, the fiducial spin prior's arbitrary upper limit strongly constrains the extent of the mass ratio distribution.

spin magnitudes (black) and larger NS spins (red). Notably, the likelihood includes comparable values for a wide range of mass ratios, including masses $m_2 < 1 M_\odot$. Contrasting the likelihood (points) to the two posterior marginals (black and red) shows how strongly the arbitrary upper limit in our fiducial *spin prior* limits the mass ratio distribution. Both extreme- q analyses nonetheless produce comparable $\tilde{\Lambda}$ posterior distributions. Due to correlations between mass ratio and $\tilde{\Lambda}$, the constraint $q < 0.6$ causes the posterior distribution of $\tilde{\Lambda}$ to systematically decrease. In Appendix C, we show that the median $\tilde{\Lambda}$ steadily decreases versus an imposed maximum mass ratio q .

These GW-only reanalyses suggest that hidden astrophysical priors change $\tilde{\Lambda}$ by roughly a factor of 2, increasing the median $\tilde{\Lambda}$ (if we require comparable mass and positive aligned spins) or decreasing it (if we require $q < 0.6$) respectively. However, because of the exponent relating $R_{1,4}$ and $\tilde{\Lambda}$, see Eq. (10), these factors of 2 propagate to a roughly 10% change in the inferred $R_{1,4}$, comparable to the statistical measurement errors usually presented for many of the individual measurements described earlier in Section II C. Figure 9 shows the cumulative distribution of $R_{1,4}$ derived from this expression and three GW-only analyses: our fiducial analysis (blue); the

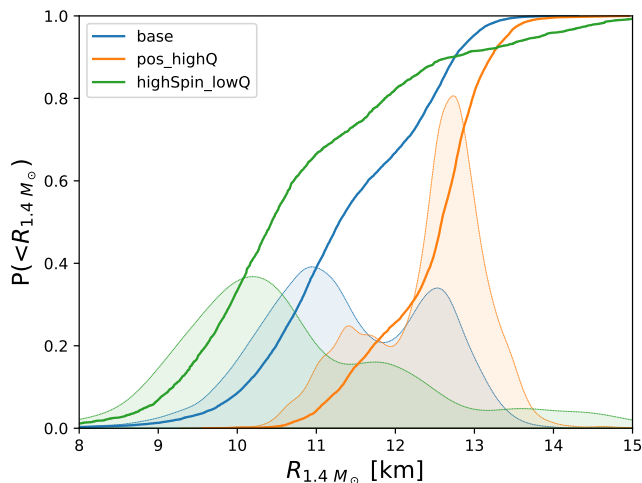


FIG. 9. **GW-derived NS radius** Nominal distribution of $R_{1.4}$ derived from Eq. (10) and three GW-only inferences of GW170817 presented in Figures 7, 8: our fiducial analysis (blue); the comparable mass positive spin analysis (orange); and the high mass ratio analysis (green). Cumulative distribution is shown in solid lines and probability distribution is shown in lighter shade.

comparable mass positive spin analysis (orange); and the high mass ratio analysis (green). Note, the bimodality in the probability distributions of the fiducial and the comparable-mass positive spin analyses arise due to bimodality in $\tilde{\Lambda}$ seen in Fig. 7.

We emphasize this simple discussion presents radius constraints directly in terms of conventional nonphysical GW priors on Λ_i , treating each as independent and uniformly distributed. These statistical errors are not informed by any EoS model families, nor even by the requirement that both NS have the same EoS. In addition, the jointly-uniform prior also produces a marginal prior distribution on $\tilde{\Lambda}$ that goes to zero as $\tilde{\Lambda}$ (i.e., $p(\tilde{\Lambda}) \propto \tilde{\Lambda}$ at small $\tilde{\Lambda}$). To facilitate visualization and downstream calculation using posterior samples, other studies have reweighted the GW-only posterior distribution for example to be uniform in $\tilde{\Lambda}$ or $R_{1.4}$; see, e.g., Figure 11 of Ref. [2]. These two priors differ substantially: using Eq. (10), a uniform prior in $\tilde{\Lambda}$ (i.e., $P(<\Lambda) = \Lambda/\Lambda_{max}$) corresponds to a cumulative prior distribution that strongly favors the largest radii (i.e., $P(<R_{1.4}) \propto R_{1.4}^6$). As our calculations employ a directly-interpolated marginal likelihood $L(X)$, not a smoothed posterior, we do not produce such an intermediate data product. Finally, even though the various model-agnostic GW priors used to construct the posterior distributions shown in Figs. 7, 8 and 9 strongly disfavor extremely small NS radii, the GW likelihood itself does not: very small Λ_i are nearly as consistent with GW170817 observations as $\Lambda_i \simeq O(100)$.

2. Joint EOS inference using GW170817

Gravitational wave measurements, currently favoring smaller radii, are by our prior's construction more informa-

tive than NICER radius constraints. As noted in Figure 1 and the associated discussion, our EoS family and prior enforce a reasonably high radius for low-mass NS leading, through regularity of the mass-radius curve and a need for large maximum mass, to EoS models that favor comparable or larger radii for typical NS. For context, comparing Figures 2 and 1, our prior favors NS radii largely consistent with the radius of J0030, including a wide range between 9 km and 16 km for a fiducial $1.4 M_{\odot}$ NS. By contrast, as surveyed in Figure 9, GW observations of GW170817 support typically smaller radii for a similar fiducial NS, with little support above 13 km in a direct interpretation of our fiducial GW analyses. As a result and as seen in previous studies, a joint analysis incorporating both galactic pulsars and GW observations finds fiducial pulsar radii comparable to the intersection of these two limits. Figure 10 shows our fiducial calculation incorporating galactic pulsar measurements, GW170817 (with our fiducial prior), and the symmetry energy, following [45]. Using similar parameterizations and observational constraints as a previous study, we find comparable inferences for the nuclear equation of state [45]. Some small differences between our inferences and prior work are expected for technical reasons; for example, we present 90% quantiles in radius at each fixed NS mass, while previous and other works adopt a NS central density prior distribution; see the appendix for further discussion.

That said, our GW analyses also demonstrate that hidden astrophysical priors have a substantial impact on the inferred NS radius. To characterize this effect, Figure 11 shows a one-dimensional scatterplot of $\ln \mathcal{L}$ versus $R_{1.4}$ using the three different GW analyses presented in Figure 9. These three analyses draw on identical RIFT marginal likelihood data, differing only in the assumed binary NS population model for mass ratio and spin. We see that the GW signal places an upper bound on the NS radius, and no strong lower bound (base). High mass ratio case (highSpin_lowQ) more strongly and more frequently penalizes higher NS radii, though some configurations with large radii are still highly likely; the overall likelihood shifts to the lowest radii. The comparable masses and positive $\chi_{i,z}$ (pos_highQ) strongly disfavours small radii and is bound on the higher radii showing most of the likelihood in a narrow range of radii on the higher end. This affirms (directly within the context of EoS inference) that astrophysical priors embedded in the GW-only analysis propagate directly into different conclusions about the nuclear EoS.

The pulsar-only likelihoods represented in Figures 2 and 4 and the (multiple) GW-only likelihoods characterized by Figure 11 show that the pulsar and GW measurements may or may not agree, with the amount of tension depending strongly on hidden astrophysical priors. In one scenario, the pulsar/GW results may be in modest tension, consistent with previously presented work. In another scenario, the two may be in good agreement, favoring radii of 13 km, if we assume GW170817 is similar to galactic pulsars. Finally, the two approaches could have strong tension, with HESS/GW favoring small radii and NICER favoring large radii, if we assume the kilonova associated with GW170817 favors asymmetric NS binaries. As an example, Figure 12 shows an analysis

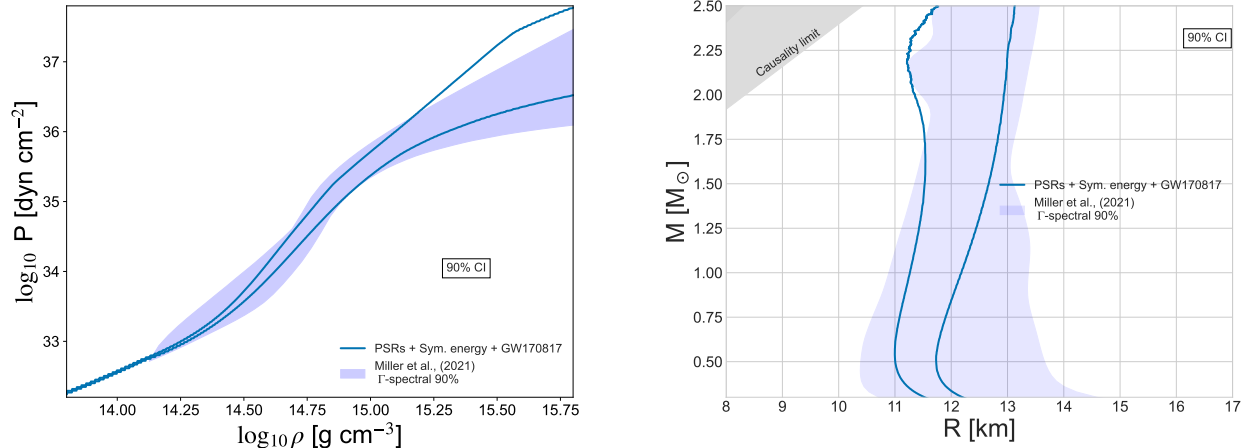


FIG. 10. **Joint EoS constraint from galactic pulsars, symmetry energy, and GW** using the Γ -spectral EoS parameterization. We also provide a benchmark analysis with the same PSRs, symmetry energy, and GW constraint, and uses the same Γ -spectral parameterization for these constraints [45].

comparable to Figure 10, excepting only the mass ratio prior ($q < 0.6$) applied for GW170817. Despite adopting the same raw GW observation and inference strategy, the same galactic pulsar measurements, and the same symmetry energy, in this scenario we would infer a notably smaller radius for most pulsars, compared to previous work.

C. On the maximum neutron star mass and pertinent information that limits it

Despite being quite restricted in form and range, our two headline equation of state families allow for EoS with very large maximum neutron star mass M_{max} ; see, e.g., Figure 13. The observations of galactic pulsars described above do not identify an upper bound on the neutron star maximum mass, explicitly or implicitly; see, e.g., [55] and references therein. Within our framework, this degeneracy manifests as a broad plateau of the likelihood that covers EoS hyperparameters including such extreme scenarios, as required by this observational constraint; see Figure 4. In our framework these EoS usually exhibit extreme behavior at high density such as their $c_s \rightarrow 1$.

Several investigations have proposed theoretically or observationally motivated limits on the EoS which would disfavor these high- M_{max} EoS. In the most extreme approach, Ref. [55] suggests that AT2017gfo’s energetics require a prompt collapse to form a black hole, limiting the neutron star maximum mass to be below $2.16^{+0.17}_{-0.15} M_{\odot}$. The bottom panel of Figure 4 shows the specific likelihood we adopt to impose this constraint, following previous work [28].

To illustrate the impact of this suggestion, Figure 14 shows updated results from our fiducial NICER analysis, now incorporating this proposed upper limit. As desired, these constraints disfavor large M_{max} . That said, taken with our other constraints, our analysis still allows for the possibility that

M_{max} is larger than the median estimate proposed by [55] using this prior information alone, and conversely still disfavors the smallest maximum masses allowed a priori due to the strongly implied minimums on M_{max} through observed NSs.

We notice that there is a shift of the M-R curve at large masses towards smaller radii which indicates that favored EoSs have a M-R that bends towards the causality limit boundary at the top left, and hence implies restrictions on EoSs. Note that these boundaries are obtained by evaluating the 90% percentile credible intervals at each mass, and hence will always have a posterior at high masses even though the EoSs with highest likelihoods do not reach such higher mass values.

As a critical side effect, these constraints on M_{max} also inform the EoS over its full dynamic range, shifting and narrowing our posterior distributions in $p(\rho)$ and $c_s(\rho)$, particularly at densities well above nuclear saturation density. Further, the soundspeed distribution narrows to higher speeds at high densities in order to compensate for the reduced stiffness at intermediate densities with lower sound speeds and lower pressures to provide with larger pressures that produce stable cores for the substantially compactified star. This results in an M-R that reach Masses of up to $\sim 2 M_{\odot}$ but does not surpass it substantially.

D. Adding the HESS source

In the main text, we have emphasized EoS inferences using conventional galactic pulsars, explicitly omitting the HESS source J1731 [83] shown in Figure 2. The inferred radius of this source is subject to strong systematic uncertainties [155]. Motivated by previous investigations to assess the impact of this event on EoS inference [156–161], with Figure 15 we show the results of EoS inference which explicitly include this event, compared with our previous results for galactic pulsars

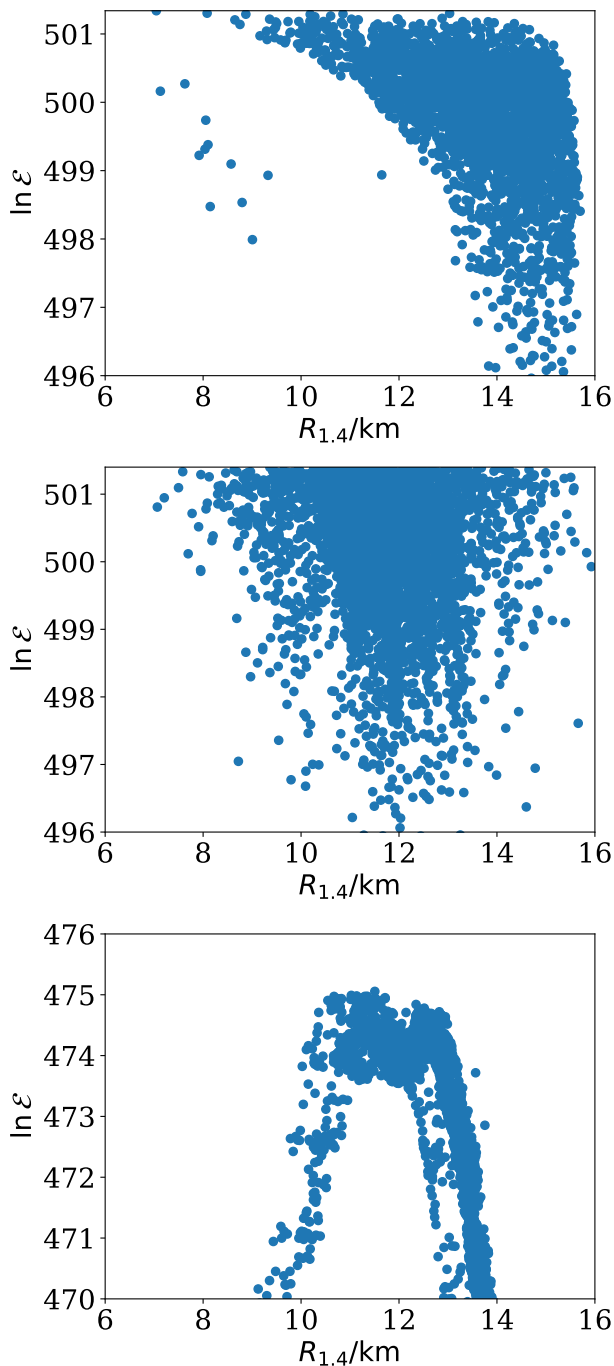


FIG. 11. **GW constraints for different astrophysical priors** Scatterplot of $\ln \mathcal{E}$ versus $R_{1.4}$ evaluated for the same three astrophysical priors for NS binaries illustrated in Figure 9. As in that figure, this representation uses evaluations drawn from the Γ -spectral EoS. *Top panel:* Likelihood for the fiducial spin and mass ratio priors (base). *Center panel:* Likelihood for the high-mass ratio prior (highSpin_lowQ). *Bottom panel:* Likelihood for the comparable-mass and positive- $\chi_{i,z}$ prior (pos_highQ).

only. Despite the nominal low maximum-likelihood mass and radius deduced for this event, when accounting for the full marginal likelihood we find GW measurements in particular are very consistent with the HESS likelihood. As a result, adding the HESS event produces only incremental changes in the EoS, both as shown here and when adding in GW and other information. In particular, the HESS observation does not seem to require exceptional EoS choices.

IV. CONCLUSIONS

In this proof-of-concept study, we have investigated how several often-observed sources of prior information propagate into statements about the nuclear equation of state. Most notably, we have demonstrated that hidden astrophysical population assumptions about the source responsible for GW170817/AT2017gfo directly propagate into substantially different conclusions, both about the radius of a fiducial neutron star and more broadly about the nuclear equation of state. In doing so, we have clarified how EoS inference *requires and explicitly depends on* strong assumptions about each pertinent neutron star population. Using two EoS parameterizations, we show how severely conclusions about the nuclear EoS can depend on parameterizations and prior choices. To concretely illuminate the impact of the prior, our hyperparameter plots indicate marginal EoS likelihoods; in every analysis, many EoSs with the highest marginal likelihood are not within our hyperparameter posterior, being disfavored by the hyperparameter prior (i.e. the priors on the two spectral parameterizations). Using the marginal likelihood to separate the impact of EoS priors, we show many EoS in our two model families are both consistent with current pulsar and GW observations but support very large NS masses. Accounting for these hidden systematics, we argue the nuclear equation of state is much less well constrained by extant observations than previously reported, particularly by investigations which stack multiple heterogeneous measurements whose relative systematics are not well understood.

The Υ -spectral model for EoS attains a higher marginal likelihood than Γ -spectral model does, implying that specific EoS samples produced by the Υ -spectral parameterization fits the observational constraint better than Γ -spectral. This is because Υ -spectral is able to produce EoSs with rapid variation in pressure with density increase as can be seen in Fig. 6. Other parameterizations such as Γ -spectral and even piecewise-polytropic do not form EoSs that can show rapid shift in slope due to the specific functional forms, and hence produce EoSs with a weaker fit. The implication of Υ -spectral parameterization is that it infers a strong phase-transition-like feature at $\sim 10^{14.5} \text{ g cm}^{-3}$.

Our conclusions are compatible with other recent reassessments of EoS-inference-adjacent observational and theoretical systematics [162]. Notably, recent re-examination of NICER observations of J0030+4051 [163] unveils a wider range of possible interpretations than the widely-used unimodal likelihood employed as input in this work. Our conclusions are also compatible with a recent galactic pulsar observations of

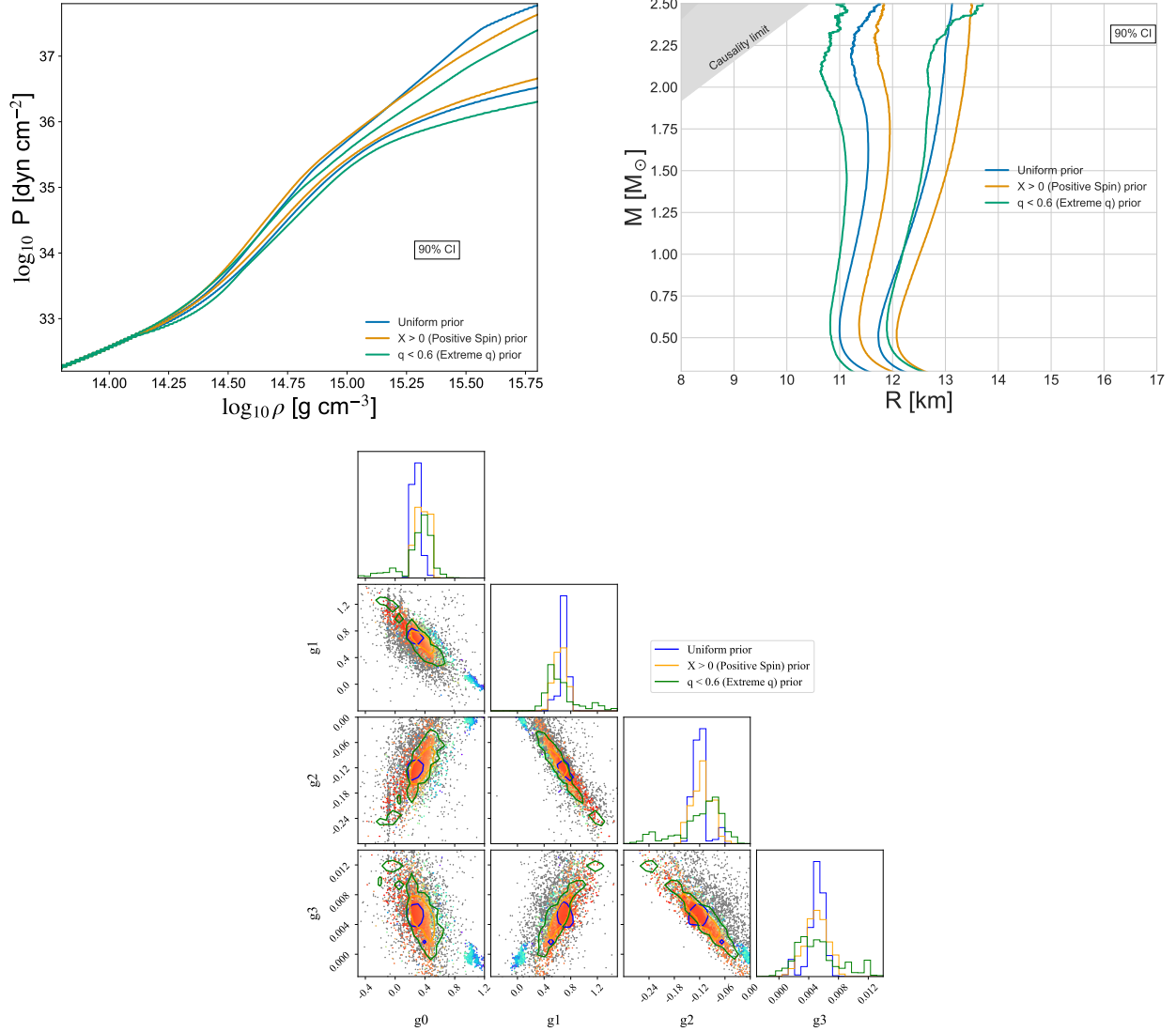


FIG. 12. Joint EoS constraint from GW, galactic pulsars, and symmetry energy, derived using Γ -spectral EoS parameterization, using three different prior assumptions about GW170817. The blue contours show results derived using the conventional 170817 prior (uniform masses); the orange requires $\chi_{i,z} > 0$; and the green requires $q < 0.6$. The analyses shown in blue have also been presented in Fig. 10. Top-left panel: 90% percentile pointwise confidence intervals for $p(\rho)$. Top-right panel: 90% percentile pointwise confidence interval for radius at each mass. Bottom panel: Γ -spectral parameter posterior distribution; we show marginal likelihood evaluations accumulated for the fiducial analysis (corresponding to the blue contours).

J0437, as summarized in an approximate analysis in Appendix E [142].

We have methodically investigated the impact on EoS inference by several external sources of information: galactic pulsar measurements of mass, mass and radius, including the HESS measurement of PSR J1731, GW measurements from GW170817, the nuclear symmetry energy implied by PREX, an upper bound on the NS maximum mass, motivated by energetics of AT2017gfo, and discussed proposed lower bounds on $\tilde{\Lambda}$ also motivated by this event. Using the (range of the) marginal log-likelihoods involved as a diagnostic of information provided by each measurement we argue that the

primary measurements (galactic pulsars, including the HESS source; GW measurements; and the symmetry energy) are remarkably consistent for our model family, particularly when allowing for systematic uncertainty in the interpretation of GW170817 due to hidden astrophysical population assumptions. This consistency suggests observations presently only coarsely constrain the EoS space, leaving limited opportunity for more flexible EoS to arrive at qualitatively different conclusions. Thus, rather than use modest tension between different observations (e.g., fiducial GW versus NICER) as a mechanism to draw narrower conclusions about the NS radius, which requires well-controlled systematics, we instead argue

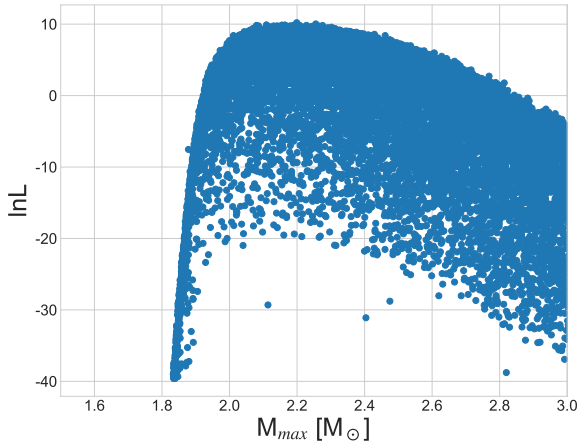
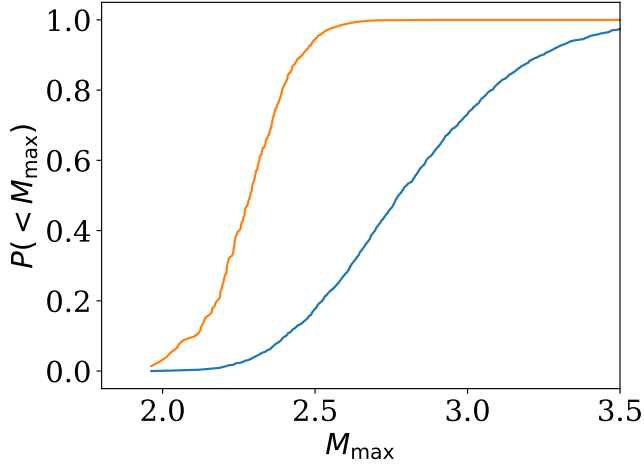


FIG. 13. **Impact of maximum nonrotating NS mass:** *Top panel:* Posterior cumulative distribution for maximum nonrotating NS mass: The fraction of EoS in our posterior with M_{\max} less than a given threshold, versus that threshold. The blue curve shows the result for our fiducial analysis with the Γ -spectral EoS with galactic pulsars and the symmetry energy, as shown in Figure 5. The orange curve shows the corresponding result after applying a nominal likelihood designed to disfavor large maximum masses, as shown in the bottom panel of Figure 4. *Bottom panel:* Marginal likelihood for different EoS, versus M_{\max} . These likelihood evaluations correspond to the orange curve in the top panel.

these tensions point to wider posterior conclusions than previously reported. Specifically, taking the union of our credible intervals between the most optimistic and pessimistic scenarios allowing for both choices for EoS family, we argue $R_{1.4}$ is between 11 km and 14 km; see Figures 10 and 6. This range is qualitatively consistent with a simple, pessimistic heuristic interpretation of how systematics limit our observations, when analyzed jointly and accounting for systematics: individual measurements' maximum likelihood estimates bracket the available range. We emphasize that these optimistic and pessimistic conclusions are driven in no small part by assumptions: which events and interpretations are used, with what EoS family and priors.

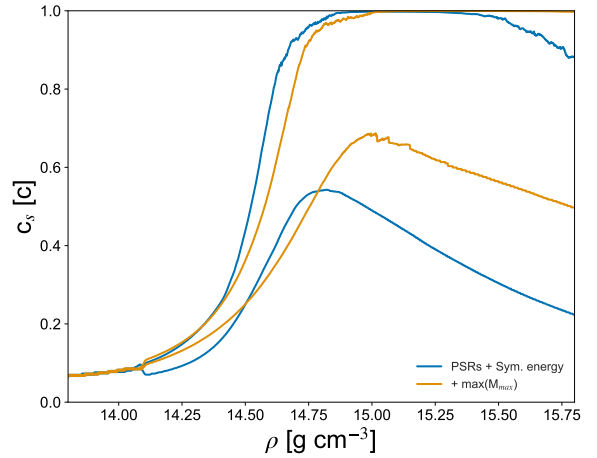
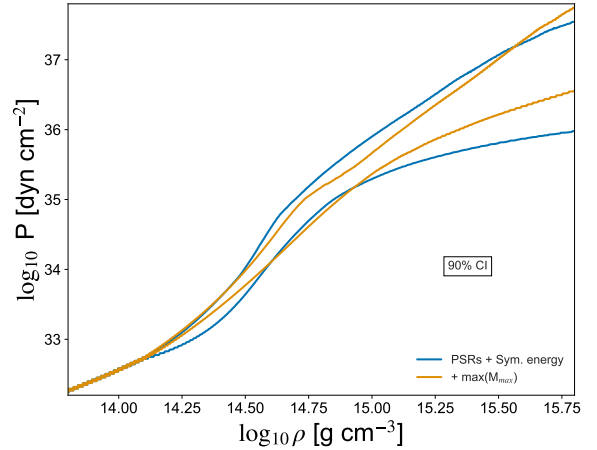
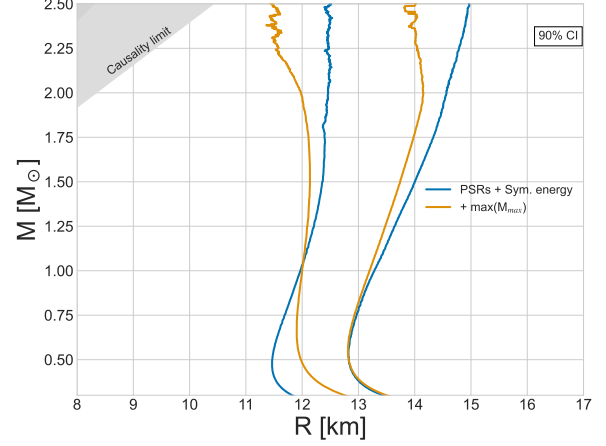


FIG. 14. **Impact of maximum mass upper limit:** Like Figure 5 – an analysis of galactic pulsar observations and the symmetry energy using the Γ -spectral EoS – but adding the upper limit on maximum mass proposed in Ref. [55].

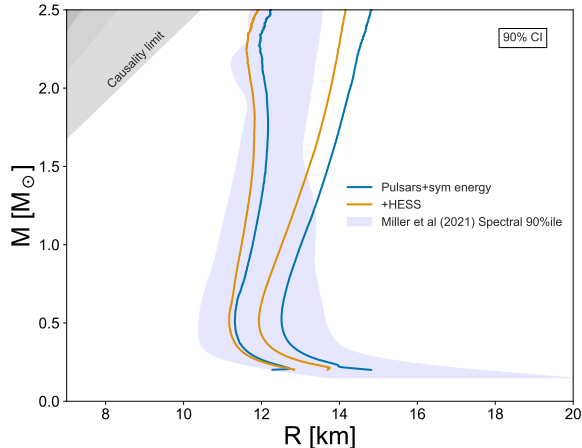


FIG. 15. **Incremental impact of HESS source:** Like Figure 5, but adding the HESS source. Except for a modest change at small radius, the overall EoS is only incrementally changed when the HESS source is included, largely at low mass. A benchmark analysis with the same PSRs and symmetry energy and uses the same Γ -spectral parameterization (also includes GW constraint) is also provided [45].

In our proof-of-concept study, we have intentionally adopted a fixed low-density EoS and thus a largely known NS radius at low mass. By adopting such a strong prior, we guarantee that low-mass NS will have the expected radius and limit the possibility that even extreme choices for EoS parameters can be in tension with observations. In other words, by fixing the low-density EoS, we increase the chance that the radius $R_{1.4}$ will be consistent with most measurements, leaving other phenomenological coordinates like M_{max} as free (and observationally unbounded) parameters. While in this work for simplicity we have adopted a fixed low-dimensional nuclear equation of state, we recognize that the high precision of future EoS constraints requires a more flexible, powerful framework that incorporates more dimensions and allows for more flexible physics like phase transitions.

To carry out our calculations, we have deployed an updated version of the RIFT pipeline capable of efficiently performing hierarchical inference with multiple objects, multiple messengers, and even flexible source populations to infer a joint equation of state. We built our analysis pipeline using *fixed* hierarchical inputs: here, approximated NICER likelihoods and high-precision marginal GW likelihoods. In future work we will generalize this pipeline to reassess the hierarchical inputs and request further refinement when needed (e.g., more marginal likelihood evaluations from the GW analysis, to better resolve the low- $\tilde{\Lambda}$ region if needed).

In Appendix B, we outline a simple estimate of how well future GW surveys can constrain the nuclear equation of state. This estimate demonstrates that most individual NS observations will directly inform the nuclear EoS, not just the loudest few. This estimate also demonstrates that, due to the strong trend of tidal deformability with radius, the least massive NS should dominate conclusions about the EoS, excepting only

that nature produces them too infrequently. Additionally, this appendix illustrates how EOS constraints will depend on two key assumptions held fixed in the main text: the assumption of a fixed, uniform NS mass distribution on the one hand, and on the number and distance distribution on the other.

The most surprising new result in our study is the strong dependence of GW-inferred tidal deformability on astrophysical prior assumptions. In addition to a fiducial analysis of GW170817, we also analyze this event using two well-motivated binary NS population models. In one model, we require GW170817 be more similar to the expected binary neutron star population, based on theoretical models for their formation: a comparable mass ratio, and with spins preferentially positively aligned with the orbital angular momentum. In the other model, designed to produce (much) larger amounts of radioactive ejecta, we require a highly asymmetric binary (potentially rapidly spinning). These two prior assumptions notably change the conclusions derived from GW170817 and hence the conclusions derived when combining this with other events. Though the latter of our two scenarios seems in tension with the long-lived galactic BNS population, we note that a rapidly-merging subpopulation could have different population properties, and offers an attractive resolution to the long-term challenge of forming r-process elements. Conversely, if we adopt a conventional galactic BNS origin for 170817 and incorporate all available measurements, we conclude $R_{1.4} \simeq 11.8 \text{ km} - 12.9 \text{ km}$.

For simplicity, in this analysis we have omitted several pertinent areas of investigations. We have notably adopted a single GW waveform model, eliding the effect of waveform modeling systematics; see Appendix C for an analysis using TEOBResumS showing that changing the waveform used for EOS inference has a small effect on baseline conclusions, in contrast to changes in the prior assumptions used. Of course, GW waveform models are only calibrated over a certain range of mass ratio, spins, and tides; for the purposes of illustration, at least one of our calculations (the use of high-mass-ratio binaries) stretches the regime of validity of the NRTidalV2 approximation. That said, our headline result – that NS population priors can strongly impact EOS inference, by changing the interpretation of GW170817 – also follows from another example, using comparable masses and positive spins, well within the calibration regime of the NRTidal method. We therefore anticipate the effect size of NS population priors to remain large even as GW waveform models improve. Also, given substantial modeling systematics, we have also only adopted toy models for the information provided from kilonova observations which limit the possible BNS mass, spin, and EoS. We have taken all existing fiducial galactic pulsar measurements at face value; reanalyses of these observations may point to larger systematics and broader posteriors than applied here [163]. Finally, we have adopted an intentionally simple EoS model family and prior, omitting often-discussed constraints available at low density (e.g., from chiral effective field theory and from state-of-the-art crust models) and at high density (e.g. that high-density EoS should asymptotically attain the perturbative-QCD limit of $c_s \rightarrow 1/\sqrt{3}$ approaching from below [164, 165]). Our choice of these simplifications

enables us to focus exclusively on the often strong and hidden impact that hidden astrophysical priors produce.

The multifactor iterative inference algorithm employed in this work is available as the `HyperPipe` component of the RIFT python software package, available at <https://pypi.org/project/RIFT/>. Instructions for this approach are available at [166]. Appendix D illustrates how the hyperpipeline accumulates information iteratively, in a manner similar to RIFT.

ACKNOWLEDGMENTS

We thank Jocelyn Read for constructive feedback during the development of this work. A.K. thanks Wolfgang Kasstaun for help with using `RePrimAnd`. We thank the NICER collaboration, in particular M. Coleman Miller, for providing us with data for certain figures. A.K. acknowledges support from National Science Foundation (NSF) Grant No. AST-1909534. ROS acknowledges support from NSF Grant No. AST-1909534, NSF Grant No. PHY-2012057, and the Simons Foundation. A.B.Y. acknowledges support from NSF Grant No. PHY-2012057. The EoS parameterizations were developed under my NSF Grant No. PHYS-2011874. We are grateful for the computational resources provided by the LIGO Laboratory, supported via National Science Foundation Grants PHY-0757058 and PHY-0823459. This material is based upon work supported by NSF’s LIGO Laboratory which is a major facility fully funded by the National Science Foundation. The code settings and data products needed to reproduce and validate our results are available on request.

Appendix A: NICER data and Gaussian approximation

The NICER data releases [167–170] provide weighted posterior samples (x_k, w_k) derived from comparing their pulse models and neutron star mass-radius combinations with observed X-ray photons. We fit a conventional two-dimensional normal distribution to these weighted samples. For J0030, which lacks any hard edges introduced by causality constraints in the (M, R) plane, we use the weighted empirical mean $\bar{x} = \sum_k w_k x_k / \sum_k w_k$ and weighted empirical covariance matrix to infer the parameters of the best-fitting gaussian. More generally, however, we optimize the mean μ and covariance matrix Σ of a standard normal distribution, according to

$$\ell(\mu, \Sigma) = \sum_k w_k \ln p(x_k | \mu, \Sigma) . \quad (\text{A1})$$

In the limit of many weighted samples constructed by importance sampling, with $w_k = L(x_k)$, the quantity ℓ will approach the KL divergence between the (truncated) Gaussian and the full posterior. As a check on our results and their stability, we repeat our analysis with fair draws from the weighted samples, using the expression above with $w_k = 1$. The best fitting normal distribution in $(R/\text{km}, M/M_\odot)$ has a mean

(13.34537396, 1.44968231) and a covariance matrix

$$\begin{bmatrix} 1.52687831 & 0.18343073 \\ 0.18343073 & 0.02778826 \end{bmatrix} .$$

Appendix B: Understanding the impact of many observations

Future instruments will enable very high precision constraints on the nuclear equation of state, through high precision constraints on $\Lambda(m)$. Starting with the pioneering work using the Fisher matrix [171], several groups have investigated how well EoS or radius constraints will improve as observations accumulate, using various levels of approximation; see, e.g., [24, 104, 172–174] and references therein. Unfortunately, many misconceptions about these constraints persist in the literature. Notably, most groups assert that the loudest few observations dominate the overall constraint. As discussed in Wysocki et al. [93] however, not only do the many weak observations make critical contributions to the overall EoS constraint, but also we must use these weak observations to help simultaneously reconstruct the NS population.

Motivated by the need for practical projections for third-generation instruments and the many-detection era, in this appendix we provide a simple ansatz allowing simple estimates showing how *statistical measurement errors* on the nuclear equation of state will improve as more observations accumulate. Our argument has five key ingredients. First, we will assume all binaries are equal mass. Second, following Ref. [136] we will assume $\Lambda(m) = \Lambda_*(m/m_*)^{-p}$ with $p = 6$, where Λ_* (the equation of state parameter to be measured with many observations) is the value of the tidal deformability at a reference mass m_* (assumed to be at or close to $m_* = 1.4 M_\odot$). Third, following the discussion in Section III.A of Ref. [93], we will argue the marginal one-dimensional measurement accuracy for the tidal deformability scales as $\sigma_\Lambda = \sigma_*(m/m_*)^{-1}$ versus binary mass, adopting a fiducial uncertainty for the faintest source used in our analysis of $\sigma_* \simeq 200$; see also, e.g., Fig. 1 in [172]. Fourth, we will assume that each independent observation’s marginal tidal deformability has a log-likelihood of the form

$$\Gamma_{**,1} = \left(\frac{\rho}{8}\right)^2 \sigma_\lambda^{-2} \left(\frac{d\Lambda}{d\Lambda_*}\right)^2 = \left(\frac{\rho}{8}\right)^2 \sigma_*^{-2} \left(\frac{m}{m_*}\right)^{2-2p} . \quad (\text{B1})$$

Fifth, we will assume the signal amplitude ρ scales with mass and luminosity distance as $(m/m_*)^{5/6} d_{L,*}/d_L$ times geometrical angular factors of order unity, i.e.

$$\rho = 8w \left(\frac{m}{m_*}\right)^{5/6} d_{L,*}/d_L . \quad (\text{B2})$$

Combining these assumptions, the net marginal likelihood from many independent observations has the form

$$\begin{aligned} \Gamma_{**,N} &= \sum_k \Gamma_{**,1,k} = N \langle \Gamma_{**,1} \rangle \\ &= N \langle w^2 \rangle \sigma_*^{-2} \left\langle \left(\frac{m}{m_*}\right)^{2/3+3-2p} \right\rangle \left\langle \left(\frac{d_{L,*}}{d_L}\right)^2 \right\rangle \quad (\text{B3}) \end{aligned}$$

where in the second line we have replaced the discrete sum by an ensemble average ($\sum_k \cdot = N\langle \cdot \rangle$) and for convenience in our ansatz we assume the angular, distance, and mass distributions of the N detected sources are independent. The average $\langle w^2 \rangle$ of the geometrical factors depends on the assumed network beampattern (and, for realistic heterogeneous networks, their duty cycle), but is well known to be $\langle w^2 \rangle = 2/5$ for the single-interferometer scenario; see Refs. [175–177] for discussion. Unless otherwise noted, for the purposes of discussion we will assume the single-interferometer beampattern factor, a uniform NS mass distribution between $1 M_\odot$ and $2 M_\odot$, and use $\left\langle \left(\frac{d_{L,*}}{d_L} \right)^2 \right\rangle \simeq 1$ as appropriate to a third-generation network. A larger value of this expression corresponds to smaller marginal measurement accuracy $\sigma_{\Lambda_*,N} \equiv 1/\sqrt{\Gamma_{**N}}$ on the fiducial tidal deformability Λ_* .

The analytic estimate provided in Eq. (B3) lets us quickly assess the relative importance of different contributions to the integral. As a concrete example, the relative contribution of sources at different distances scales as the relative contributions to $\langle 1/d_L^2 \rangle$, which under the conventional assumption of an event rate comparable to comoving volume has a critical contribution from the *weakest* sources available to the population average. For a Euclidean distribution of sources out to the maximum detectable distance $d_{L,*}$, within our ansatz we find $\langle (d_{L,*}/d_L)^2 \rangle = 3$. Weak sources play an even more important role if sources occur more frequently at higher redshift, as expected given the increasing star formation rate with redshift. In the extreme limit of strong redshift dependence and cosmological factors, we expect $\langle (d_{L,*}/d_L)^2 \rangle \simeq 1$. The primary limitation of this interpretation is the implicit assumption of a Gaussian joint likelihood, which only applies for loud signals (e.g., comparable to GW170817). Even after restricting our calculation to sources louder than ρ_c , the detection rate of pertinent sources is only reduced by of order $(8/\rho_c)^3$. For third-generation instruments with $O(10^5)$ sources, many thousands must still make important contributions, even for the most conservative choices for ρ_c . Moreover, once in the Gaussian-likelihood regime, our calculation scales much more slowly than the naive Euclidean factor, only as $N\langle (d_{L,*}/d_L)^2 \rangle$.

Our expression provides an even stronger conclusion about the relative importance of different parts of the mass distribution: the lowest mass binaries overwhelmingly dominate the mass average $\langle m^{11/3-2p} \rangle \simeq \langle m^{-8} \rangle$ (more precisely $= \frac{1-2-(8-2/3)}{9-2/3}$ for the average for a uniform mass distribution from $1 M_\odot$ to $2 M_\odot$). In retrospect, the lowest mass binaries must dominate: $\Lambda(m)$ is vastly larger at the lowest allowed masses. If any binaries exist at these masses their observations will dominate our constraints on the equation of state because their large tidal effects will be easily differentiated from the noise.

Our expression implies the measurement accuracy $\sigma_{\Lambda_*,N}$ from combining N measurements will be roughly

$$\sigma_{\Lambda_*,N} \simeq 200/\sqrt{N} \quad (\text{B4})$$

Our simple estimate is comparable to (but calibrated above to be slightly more optimistic than) detailed calculations pro-

duced in other studies [104, 172, 178]; for example, ref. [104] argues the 90% credible interval is $\Delta\Lambda_* \simeq 910/\sqrt{N}$ and thus that the comparable 68% credible interval would be $520/\sqrt{N}$. The aforementioned measurement accuracy on Λ_* implies a relative measurement accuracy on $\ln R_*$ of $\Lambda_*^{-1} |d \ln R_*/d \ln \Lambda_*| / \sqrt{\Gamma_{**N}}$. To evaluate this expression and put the result in context, we'll assume for the purposes of illustration the MPA1 equation of state, which produces for $m_* = 1.4 M_\odot$ the fiducial pair $(\Lambda_*, R_*/\text{km}) = (513, 12.5)$. For simplicity again following Zhao and Lattimer [136], we can evaluate this change-of-variable expression by adopting the same scaling $\Lambda = a(m/R)^{-p}$ assumed above for some constant $a \simeq 0.0085$, so $d \ln R_*/d \ln \Lambda_* = p$. We therefore estimate the measurement accuracy $\sigma_{R_*,N}$ in R_* produced by stacking N measurements to be

$$\sigma_{R_*,N} \simeq R_* \frac{p\sigma_*}{\Lambda_* \sqrt{\langle w^2 \rangle N \langle (d_{L,*}/d_L)^2 \rangle \left\langle \left(\frac{m}{m_*} \right)^{2/3+3-2p} \right\rangle}} \quad (\text{B5})$$

$$\simeq 5\text{km}/\sqrt{N} \quad (\text{B6})$$

which is close to (but slightly wider than) the corresponding estimate presented in [104]. Our simple estimates can be easily updated (and compared to the latest best-fit value Λ_*) as our understanding of the NS mass distribution and measurement accuracy improves. They can likewise be easily updated to include both GW and X-ray observations adding in quadrature.

Our analysis in this appendix suggests important trends in tension with previous preliminary investigations. Many groups over several years have argued that only the loudest handful of observations will dominate overall EoS inference [171, 179]. Our analytic argument suggests a comparable and potentially even dominant contribution from more numerous fainter events.

In the discussion in this appendix, we have only provided estimates for the statistical accuracy $\sigma_{\Lambda_*,N}$ and $\sigma_{R_*,N}$ for the tidal deformability and radius of a fiducial neutron star, respectively, after combining N events. Given proposed network sensitivity models and reference, these expressions can be immediately translated to the operating time needed to constrain these quantities to any target precision. For example, in terms of the proposed detection rate of useful events (scaled to $10^5/\text{yr}$, assuming all events contribute) we find for the simple estimates discussed here that a target accuracy of $\Delta R_* = 10$ m requires an observing time scaling with event rate and fiducial neutron star radius as

$$T_R = R_d^{-1} (\sigma_{R_*,N}/\Delta R_*)^2 \simeq 2.5\text{yr} (R_d \text{yr}/10^5)^{-1} (R_*/12.5\text{km})^2. \quad (\text{B7})$$

Appendix C: More alternate perspectives on GW170817

In this appendix, we describe a few supplementary analyses of GW170817 which complement the material presented in the text.

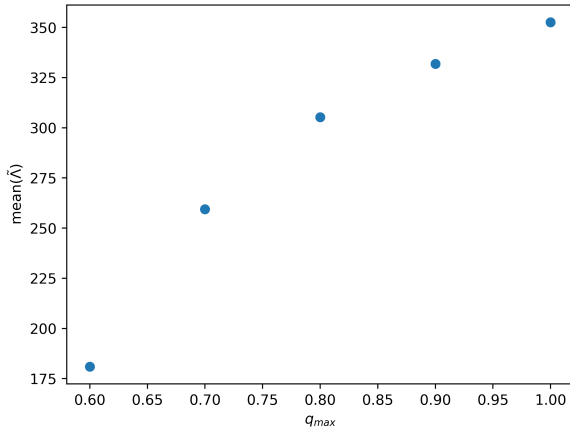


FIG. 16. Median $\tilde{\lambda}$ versus q_{\max} . In this figure, parameter inferences are performed with the same fiducial mass, spin, and tidal deformability priors as adopted in Figure 7, except that the mass ratio is constrained to be less than q_{\max} .

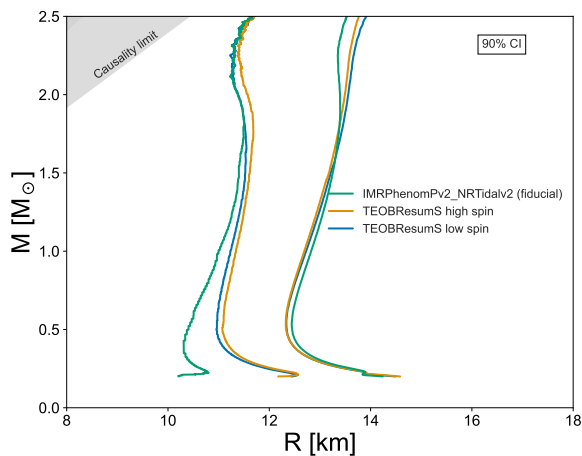


FIG. 17. Mass-radius posterior distribution derived from alternative parameter inferences of GW170817 using a different waveform model

Figure 16 shows the median $\tilde{\lambda}$ obtained from a one-parameter family of interpretations of GW170817, which al-

low for binary mass ratios $q < q_{\max}$ that range between the two fiducial extremes presented in the text.

Figure 17 shows the results of an analysis that incorporates an alternative interpretation of GW170817 performed by Lange et al. (in prep), obtained by comparing the TEOBResumS waveform model to the data. The differences in interpretation reported there propagate to modest differences in the mass-radius posterior distribution using the baseline, broad NS population prior.

Appendix D: Hyperpipeline examples

In Section II G we presented our iterative strategy for hyperparameter inference. This approach has been used for GW source parameter inference with RIFT as well as the equation of state which are presented in the Section III. Here, we provide illustrations showing how our iterative strategy works within the context of EoS hyperparameter inference.

As an example, Figure 18 shows 90% credible intervals estimated at each stage of one of our analyses, along with (in color) the marginal likelihoods accumulated during the analysis. Initial grid is an initial guess made during this work, however the pipeline starts exploring regions to obtain a more complete picture of the posterior. By the 5th, 6th, and 7th iteration the posterior estimation does not change significantly, leading us to a converged posterior distribution.

Appendix E: NICER PSR-J0437

One of the NICER collaboration groups announced the observational constraints for PSR-J0437 [142]. The pulsar has a strong a-priori mass constraint from radio observations [180]. The full posterior data release has not occurred, however, here we apply this pulsar’s separate 90% credible intervals for its mass and radius and can construct an approximate Gaussian posterior to explore its effect on the EoS. The reported Radius is $R = 11.36^{+0.95}_{-0.63}$ km and $M = 1.418 \pm 0.037 M_{\odot}$. For this preliminary application, we employ the constraints as a Gaussian with $R = 11.36 \pm 0.95$ km and $M = 1.418 \pm 0.037 M_{\odot}$.

Figure 19 displays the posterior Mass-Radius 90% credible interval shown earlier in Fig. 10, and a new posterior obtained upon applying the mass-radius constraint for PSR-J0437. Again, we notice on this preliminary study, the impact of this additional source on the M-R posterior is very minimal.

-
- [1] The LIGO Scientific Collaboration, the Virgo Collaboration, B. P. Abbott, R. Abbott, T. D. Abbott, F. Acernese, K. Ackley, C. Adams, T. Adams, P. Addesso, and et al., GW170817: Observation of gravitational waves from a binary neutron star inspiral, *Phys. Rev. Lett.* **119**, 161101 (2017).
- [2] The LIGO Scientific Collaboration, the Virgo Collaboration, B. P. Abbott, R. Abbott, T. D. Abbott, F. Acernese, K. Ackley, C. Adams, T. Adams, P. Addesso, and et al., Properties of the Binary Neutron Star Merger GW170817, *Phys. Rev. X* **9**,

011001 (2019).

- [3] The LIGO Scientific Collaboration, the Virgo Collaboration, B. P. Abbott, R. Abbott, T. D. Abbott, F. Acernese, K. Ackley, C. Adams, T. Adams, P. Addesso, and et al., GW170817: Measurements of neutron star radii and equation of state, *Phys. Rev. Lett.* **121**, 161101 (2018).
- [4] K. Chatziioannou, Neutron-star tidal deformability and equation-of-state constraints, *Gen. Relativ. Gravit.* **52**, 109 (2020).

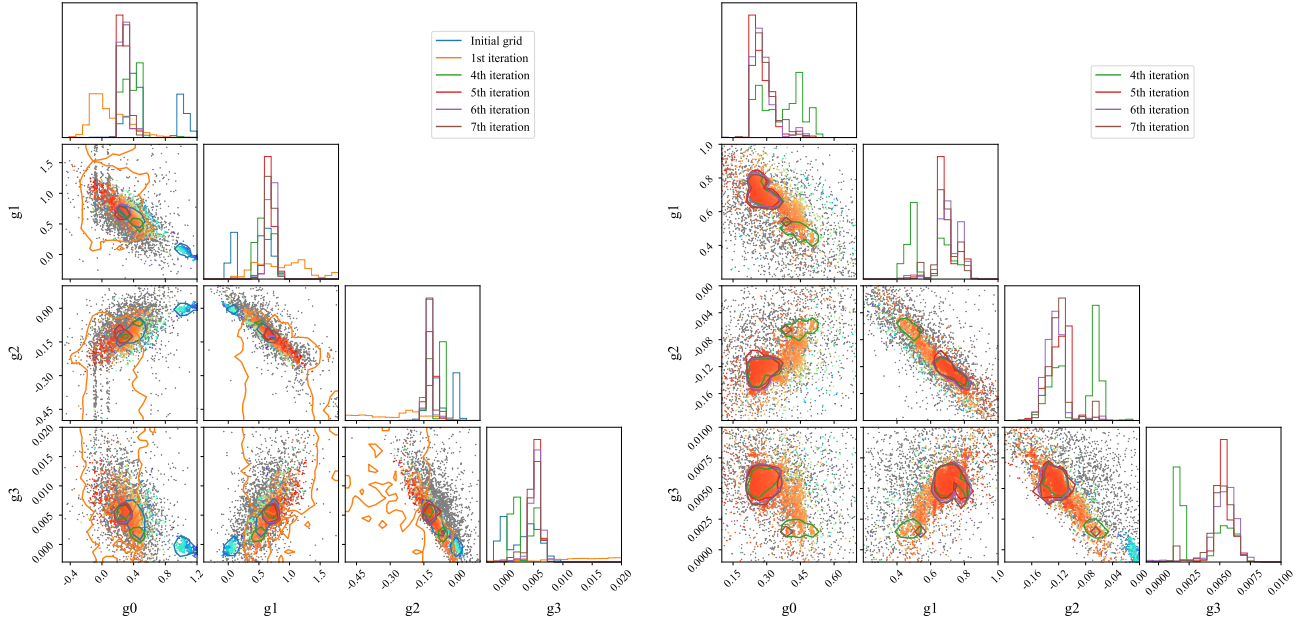


FIG. 18. Hyperparameter corner plot: Joint EoS constraint from galactic pulsars, symmetry energy, and GW using the Γ -spectral EoS parameterization (the hyperparameters that lead to Fig. 10). The right panel zooms into the last four iterations in the first panel.

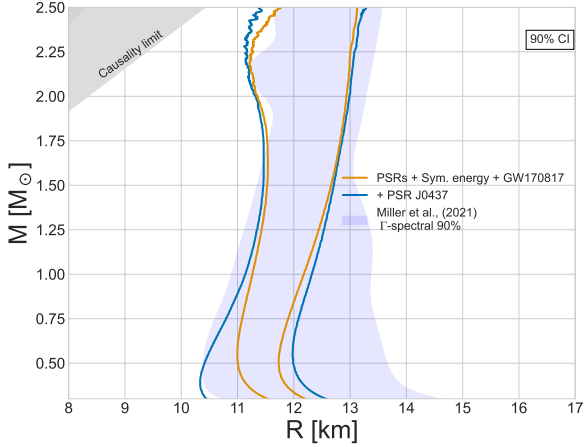


FIG. 19. Mass-Radius posterior comparison without (Orange) and with (Blue) the approximate PSR-J0437 posteriors in the inference.

- [5] P. Landry, R. Essick, and K. Chatziioannou, Nonparametric constraints on neutron star matter with existing and upcoming gravitational wave and pulsar observations, *Phys. Rev. D* **101**, 123007 (2020).
- [6] E. R. Most, A. Motornenko, J. Steinheimer, V. Dexheimer, M. Hanauske, L. Rezzolla, and H. Stoecker, Probing neutron-star matter in the lab: Similarities and differences between binary mergers and heavy-ion collisions, *Phys. Rev. D* **107**, 043034 (2023).
- [7] B. T. Reed, F. J. Fattoyev, C. J. Horowitz, and J. Piekarewicz, Implications of PREX-2 on the Equation of State of Neutron-

- Rich Matter, *Phys. Rev. Lett.* **126**, 172503 (2021).
- [8] R. Essick, I. Tews, P. Landry, and A. Schwenk, Astrophysical Constraints on the Symmetry Energy and the Neutron Skin of Pb208 with Minimal Modeling Assumptions, *Phys. Rev. Lett.* **127**, 192701 (2021).
- [9] M. Agathos, J. Meidam, W. Del Pozzo, T. G. F. Li, M. Tompitak, J. Veitch, S. Vitale, and C. Van Den Broeck, Constraining the neutron star equation of state with gravitational wave signals from coalescing binary neutron stars, *Phys. Rev. D* **92**, 023012 (2015).
- [10] B. D. Lackey and L. Wade, Reconstructing the neutron-star equation of state with gravitational-wave detectors from a realistic population of inspiralling binary neutron stars, *Phys. Rev. D* **91**, 043002 (2015).
- [11] D. Alvarez-Castillo, A. Ayriyan, S. Benic, D. Blaschke, H. Grigorian, and S. Typel, New class of hybrid EoS and Bayesian M-R data analysis, *Eur. Phys. J. A* **52**, 69 (2016).
- [12] B. Margalit and B. D. Metzger, Constraining the Maximum Mass of Neutron Stars From Multi-Messenger Observations of GW170817, *Astrophys. J.* **850**, L19 (2017).
- [13] E. Annala, T. Gorda, A. Kurkela, and A. Vuorinen, Gravitational-wave constraints on the neutron-star-matter Equation of State, *Phys. Rev. Lett.* **120**, 172703 (2018).
- [14] E. R. Most, L. R. Weih, L. Rezzolla, and J. Schaffner-Bielich, New constraints on radii and tidal deformabilities of neutron stars from GW170817, *Phys. Rev. Lett.* **120**, 261103 (2018).
- [15] D. Radice, A. Perego, F. Zappa, and S. Bernuzzi, GW170817: Joint Constraint on the Neutron Star Equation of State from Multimessenger Observations, *Astrophys. J.* **852**, L29 (2018).
- [16] L. Rezzolla, E. R. Most, and L. R. Weih, Using gravitational-wave observations and quasi-universal relations to constrain the maximum mass of neutron stars, *Astrophys. J. Lett.* **852**, L25 (2018).
- [17] T. E. Riley, G. Raaijmakers, and A. L. Watts, On parametrized cold dense matter equation-of-state inference, *Mon. Not. Roy.*

- Astron. Soc.* **478**, 1093 (2018).
- [18] I. Tews, J. Margueron, and S. Reddy, Critical examination of constraints on the equation of state of dense matter obtained from GW170817, *Phys. Rev. C* **98**, 045804 (2018).
- [19] S. K. Greif, G. Raaijmakers, K. Hebeler, A. Schwenk, and A. L. Watts, Equation of state sensitivities when inferring neutron star and dense matter properties, *Mon. Not. Roy. Astron. Soc.* **485**, 5363 (2019).
- [20] K. Kiuchi, K. Kyutoku, M. Shibata, and K. Taniguchi, Revisiting the lower bound on tidal deformability derived by AT 2017gfo, *Astrophys. J. Lett.* **876**, L31 (2019).
- [21] P. Landry and R. Essick, Nonparametric inference of the neutron star equation of state from gravitational wave observations, *Phys. Rev. D* **99**, 084049 (2019).
- [22] M. Shibata, E. Zhou, K. Kiuchi, and S. Fujibayashi, Constraint on the maximum mass of neutron stars using GW170817 event, *Phys. Rev. D* **100**, 023015 (2019).
- [23] C. D. Capano, I. Tews, S. M. Brown, B. Margalit, S. De, S. Kumar, D. A. Brown, B. Krishnan, and S. Reddy, Stringent constraints on neutron-star radii from multimessenger observations and nuclear theory, *Nature Astronomy* **4**, 625 (2020).
- [24] P. T. H. Pang, T. Dietrich, I. Tews, and C. Van Den Broeck, Parameter estimation for strong phase transitions in supranuclear matter using gravitational-wave astronomy, *Phys. Rev. Res.* **2**, 033514 (2020).
- [25] N.-B. Zhang and B.-A. Li, Constraints on the Muon Fraction and Density Profile in Neutron Stars, *Astrophys. J.* **893**, 61 (2020).
- [26] R. Essick, I. Tews, P. Landry, S. Reddy, and D. E. Holz, Direct Astrophysical Tests of Chiral Effective Field Theory at Supranuclear Densities, *Phys. Rev. C* **102**, 055803 (2020).
- [27] G. Raaijmakers, S. K. Greif, T. E. Riley, T. Hinderer, K. Hebeler, A. Schwenk, A. L. Watts, S. Nisanke, S. Guillot, J. M. Lattimer, and R. M. Ludlam, Constraining the Dense Matter Equation of State with Joint Analysis of NICER and LIGO/Virgo Measurements, *Astrophys. J. Lett.* **893**, L21 (2020).
- [28] T. Dietrich, M. W. Coughlin, P. T. H. Pang, M. Bulla, J. Heinzel, L. Issa, I. Tews, and S. Antier, Multimessenger constraints on the neutron-star equation of state and the Hubble constant, *Science* **370**, 1450 (2020).
- [29] M. Cierniak and D. Blaschke, The special point on the hybrid star mass-radius diagram and its multi-messenger implications, *European Physical Journal Special Topics* **229**, 3663 (2020).
- [30] B.-A. Li and M. Magno, Curvature-slope correlation of nuclear symmetry energy and its imprints on the crust-core transition, radius, and tidal deformability of canonical neutron stars, *Phys. Rev. C* **102**, 045807 (2020).
- [31] W.-J. Xie and B.-A. Li, Bayesian inference of the dense-matter equation of state encapsulating a first-order hadron-quark phase transition from observables of canonical neutron stars, *Phys. Rev. C* **103**, 035802 (2021).
- [32] M. Al-Mamun, A. W. Steiner, J. Nättilä, J. Lange, R. O’Shaughnessy, I. Tews, S. Gandolfi, C. Heinke, and S. Han, Combining Electromagnetic and Gravitational-Wave Constraints on Neutron-Star Masses and Radii, *Phys. Rev. Lett.* **126**, 061101 (2021).
- [33] F. Özel and P. Freire, Masses, Radii, and the Equation of State of Neutron Stars, *Annu. Rev. Astron. Astrophys.* **54**, 401 (2016).
- [34] S. Bogdanov, C. O. Heinke, F. Özel, and T. Güver, Neutron Star Mass-Radius Constraints of the Quiescent Low-mass X-Ray Binaries X7 and X5 in the Globular Cluster 47 Tuc, *Astrophys. J.* **831**, 184 (2016).
- [35] A. W. Steiner, C. O. Heinke, S. Bogdanov, C. Li, W. C. G. Ho, A. Bahramian, and S. Han, Constraining the Mass and Radius of Neutron Stars in Globular Clusters, *Mon. Not. Roy. Astron. Soc.* **476**, 421 (2018).
- [36] D. Farrell, P. Baldi, J. Ott, A. Ghosh, A. W. Steiner, A. Kaviratkar, L. Lindblom, D. Whiteson, and F. Weber, Deducing neutron star equation of state parameters directly from telescope spectra with uncertainty-aware machine learning, *J. Cosmol. Astropart. Phys.* **2023**, 016 (2023).
- [37] M. C. Miller *et al.*, PSR J0030+0451 Mass and Radius from *NICER* Data and Implications for the Properties of Neutron Star Matter, *Astrophys. J. Lett.* **887**, L24 (2019).
- [38] T. E. Riley *et al.*, A *NICER* View of PSR J0030+0451: Millisecond Pulsar Parameter Estimation, *Astrophys. J. Lett.* **887**, L21 (2019).
- [39] G. Raaijmakers *et al.*, A *NICER* view of PSR J0030+0451: Implications for the dense matter equation of state, *Astrophys. J. Lett.* **887**, L22 (2019).
- [40] A. V. Bilous *et al.*, A *NICER* view of PSR J0030+0451: evidence for a global-scale multipolar magnetic field, *Astrophys. J. Lett.* **887**, L23 (2019).
- [41] S. Guillot, M. Kerr, P. S. Ray, S. Bogdanov, S. Ransom, J. S. Deneva, Z. Arzoumanian, P. Bult, D. Chakrabarty, K. C. Gendreau, W. C. G. Ho, G. K. Jaiswal, C. Malacaria, M. C. Miller, T. E. Strohmayer, M. T. Wolff, K. S. Wood, N. A. Webb, L. Guillemot, I. Cognard, and G. Theureau, *NICER* X-Ray Observations of Seven Nearby Rotation-powered Millisecond Pulsars, *Astrophys. J. Lett.* **887**, L27 (2019).
- [42] S. Bogdanov *et al.*, Constraining the Neutron Star Mass–Radius Relation and Dense Matter Equation of State with *NICER*. I. The Millisecond Pulsar X-Ray Data Set, *Astrophys. J. Lett.* **887**, L25 (2019).
- [43] S. Bogdanov *et al.*, Constraining the Neutron Star Mass–Radius Relation and Dense Matter Equation of State with *NICER*. II. Emission from Hot Spots on a Rapidly Rotating Neutron Star, *Astrophys. J. Lett.* **887**, L26 (2019).
- [44] S. Bogdanov, A. J. Dittmann, W. C. G. Ho, F. K. Lamb, S. Mahmoodifar, M. C. Miller, S. M. Morsink, T. E. Riley, T. E. Strohmayer, A. L. Watts, D. Choudhury, S. Guillot, A. K. Harding, P. S. Ray, Z. Wadiasingh, M. T. Wolff, C. B. Markwardt, Z. Arzoumanian, and K. C. Gendreau, Constraining the Neutron Star Mass-Radius Relation and Dense Matter Equation of State with *NICER*. III. Model Description and Verification of Parameter Estimation Codes, *Astrophys. J. Lett.* **914**, L15 (2021).
- [45] M. C. Miller *et al.*, The Radius of PSR J0740+6620 from *NICER* and XMM-Newton Data, *Astrophys. J. Lett.* **918**, L28 (2021).
- [46] T. E. Riley *et al.*, A *NICER* View of the Massive Pulsar PSR J0740+6620 Informed by Radio Timing and XMM-Newton Spectroscopy, *Astrophys. J. Lett.* **918**, L27 (2021).
- [47] G. Raaijmakers, S. K. Greif, K. Hebeler, T. Hinderer, S. Nisanke, A. Schwenk, T. E. Riley, A. L. Watts, J. M. Lattimer, and W. C. G. Ho, Constraints on the Dense Matter Equation of State and Neutron Star Properties from *NICER*’s Mass-Radius Estimate of PSR J0740+6620 and Multimessenger Observations, *Astrophys. J. Lett.* **918**, L29 (2021).
- [48] J.-E. Christian and J. Schaffner-Bielich, Twin Stars and the Stiffness of the Nuclear Equation of State: Ruling Out Strong Phase Transitions below $1.7 n_0$ with the New *NICER* Radius Measurements, *Astrophys. J. Lett.* **894**, L8 (2020).
- [49] G. Raaijmakers *et al.*, Constraining the dense matter equation of state with joint analysis of *NICER* and LIGO/Virgo mea-

- surements, *Astrophys. J. Lett.* **893**, L21 (2020).
- [50] I. Legred, K. Chatziioannou, R. Essick, S. Han, and P. Landry, Impact of the psr J0740+6620 radius constraint on the properties of high-density matter, *Phys. Rev. D* **104**, 063003 (2021).
- [51] P. T. H. Pang, I. Tews, M. W. Coughlin, M. Bulla, C. Van Den Broeck, and T. Dietrich, Nuclear Physics Multimessenger Astrophysics Constraints on the Neutron Star Equation of State: Adding NICER’s PSR J0740+6620 Measurement, *Astrophys. J.* **922**, 14 (2021).
- [52] S. De, D. Finstad, J. M. Lattimer, D. A. Brown, E. Berger, and C. M. Biwer, Tidal Deformabilities and Radii of Neutron Stars from the Observation of GW170817, *Phys. Rev. Lett.* **121**, 091102 (2018), [Erratum: *Phys. Rev. Lett.* 121,no.25,259902(2018)].
- [53] D. Radice, A. Perego, F. Zappa, and S. Bernuzzi, GW170817: Joint constraint on the Neutron Star Equation of State from Multimessenger Observations, *Astrophys. J. Lett.* **852**, L29 (2018).
- [54] A. Bauswein, O. Just, H.-T. Janka, and N. Stergioulas, Neutron-star Radius Constraints from GW170817 and Future Detections, *Astrophys. J. Lett.* **850**, L34 (2017).
- [55] L. Rezzolla, E. R. Most, and L. R. Weih, Using Gravitational-wave Observations and Quasi-universal Relations to Constrain the Maximum Mass of Neutron Stars, *Astrophys. J. Lett.* **852**, L25 (2018).
- [56] M. W. Coughlin *et al.*, Constraints on the neutron star equation of state from AT2017gfo using radiative transfer simulations, *Mon. Not. Roy. Astron. Soc.* **480**, 3871 (2018).
- [57] M. W. Coughlin, T. Dietrich, B. Margalit, and B. D. Metzger, Multimessenger Bayesian parameter inference of a binary neutron star merger, *Mon. Not. Roy. Astron. Soc.* **489**, L91 (2019).
- [58] C. Raithel, F. Özel, and D. Psaltis, Tidal deformability from GW170817 as a direct probe of the neutron star radius, *Astrophys. J.* **857**, L23 (2018).
- [59] M. Ruiz, S. L. Shapiro, and A. Tsokaros, GW170817, general relativistic magnetohydrodynamic simulations, and the neutron star maximum mass, *Phys. Rev. D* **97**, 021501 (2018).
- [60] E. R. Most, L. J. Papenfort, V. Dexheimer, M. Hanauske, S. Schramm, H. Stoecker, and L. Rezzolla, Signatures of quark-hadron phase transitions in general-relativistic neutron-star mergers, *Phys. Rev. Lett.* **122**, 061101 (2019).
- [61] A. Nathanail, E. R. Most, and L. Rezzolla, GW170817 and GW190814: Tension on the Maximum Mass, *Astrophys. J. Lett.* **908**, L28 (2021).
- [62] H. Sotani, K. D. Kokkotas, and N. Stergioulas, Neutron star mass-radius constraints using the high-frequency quasi-periodic oscillations of GRB 200415A, *Astron. Astrophys.* **676**, A65 (2023).
- [63] E. Thrane and C. Talbot, An introduction to Bayesian inference in gravitational-wave astronomy: Parameter estimation, model selection, and hierarchical models, *Publ. Astron. Soc. Aust.* **36**, e010 (2019).
- [64] V. Nedora, S. Bernuzzi, D. Radice, B. Daszuta, A. Endrizzi, A. Perego, A. Prakash, M. Safarzadeh, F. Schianchi, and D. Logoteta, Numerical Relativity Simulations of the Neutron Star Merger GW170817: Long-term Remnant Evolutions, Winds, Remnant Disks, and Nucleosynthesis, *Astrophys. J.* **906**, 98 (2021).
- [65] D. Radice, S. Bernuzzi, and A. Perego, The Dynamics of Binary Neutron Star Mergers and GW170817, *Annu. Rev. Nucl. Part. Sci.* **70**, annurev (2020).
- [66] O. Korobkin, R. T. Wollaeger, C. L. Fryer, A. L. Hungerford, S. Rosswog, C. J. Fontes, M. R. Mumpower, E. A. Chase, W. P. Even, J. Miller, G. W. Misch, and J. Lippuner, Axisymmetric Radiative Transfer Models of Kilonovae, *Astrophys. J.* **910**, 116 (2021).
- [67] A. Kedia, M. Ristic, R. O’Shaughnessy, A. B. Yelikar, R. T. Wollaeger, O. Korobkin, E. A. Chase, C. L. Fryer, and C. J. Fontes, Surrogate light curve models for kilonovae with comprehensive wind ejecta outflows and parameter estimation for at2017gfo, *Phys. Rev. Res.* **5**, 013168 (2023).
- [68] M. Ristic, E. Champion, R. O’Shaughnessy, R. Wollaeger, O. Korobkin, E. A. Chase, C. L. Fryer, A. L. Hungerford, and C. J. Fontes, Interpolating detailed simulations of kilonovae: Adaptive learning and parameter inference applications, *Phys. Rev. Res.* **4**, 013046 (2022).
- [69] C. A. Raithel, F. Özel, and D. Psaltis, From Neutron Star Observables to the Equation of State. II. Bayesian Inference of Equation of State Pressures, *Astrophys. J.* **844**, 156 (2017).
- [70] C. A. Raithel, F. Özel, and D. Psaltis, Optimized Statistical Approach for Comparing Multi-messenger Neutron Star Data, *Astrophys. J.* **908**, 103 (2021).
- [71] I. Legred, K. Chatziioannou, R. Essick, and P. Landry, Implicit correlations within phenomenological parametric models of the neutron star equation of state, *Phys. Rev. D* **105**, 043016 (2022).
- [72] C. Drischler, J. W. Holt, and C. Wellenhofer, Chiral Effective Field Theory and the High-Density Nuclear Equation of State, *Annu. Rev. Nucl. Part. Sci.* **71**, 403 (2021).
- [73] J. M. Lattimer, Neutron Stars and the Nuclear Matter Equation of State, *Annu. Rev. Nucl. Part. Sci.* **71**, 433 (2021).
- [74] D. Mroczek, M. C. Miller, J. Noronha-Hostler, and N. Yunes, Nontrivial features in the speed of sound inside neutron stars, *Phys. Rev. D* **110**, 123009 (2024).
- [75] C. A. Raithel and E. R. Most, Degeneracy in the Inference of Phase Transitions in the Neutron Star Equation of State from Gravitational Wave Data, *Phys. Rev. Lett.* **130**, 201403 (2023).
- [76] L. Lindblom, Spectral Representations of Neutron-Star Equations of State, *Phys. Rev. D* **82**, 103011 (2010).
- [77] L. Lindblom, Causal Representations of Neutron-Star Equations of State, *Phys. Rev. D* **97**, 123019 (2018).
- [78] L. Lindblom, Improved spectral representations of neutron-star equations of state, *Phys. Rev. D* **105**, 063031 (2022).
- [79] P. Landry and J. S. Read, The Mass Distribution of Neutron Stars in Gravitational-wave Binaries, *Astrophys. J. Lett.* **921**, L25 (2021).
- [80] J. Antoniadis, P. C. Freire, N. Wex, T. M. Tauris, R. S. Lynch, *et al.*, A Massive Pulsar in a Compact Relativistic Binary, *Science* **340**, 1233232 (2013).
- [81] Z. Arzoumanian, A. Brazier, S. Burke-Spolaor, S. Chamberlin, S. Chatterjee, B. Christy, J. M. Cordes, N. J. Cornish, F. Crawford, H. Thankful Cromartie, K. Crowter, M. E. DeCesar, P. B. Demorest, T. Dolch, J. A. Ellis, R. D. Ferdman, E. C. Ferrara, E. Fonseca, N. Garver-Daniels, P. A. Gentile, D. Halmrast, E. A. Huerta, F. A. Jenet, C. Jessup, G. Jones, M. L. Jones, D. L. Kaplan, M. T. Lam, T. J. W. Lazio, L. Levin, A. Lommen, D. R. Lorimer, J. Luo, R. S. Lynch, D. Madison, A. M. Matthews, M. A. McLaughlin, S. T. McWilliams, C. Mingarelli, C. Ng, D. J. Nice, T. T. Pennucci, S. M. Ransom, P. S. Ray, X. Siemens, J. Simon, R. Spiewak, I. H. Stairs, D. R. Stinebring, K. Stovall, J. K. Swiggum, S. R. Taylor, M. Vallisneri, R. van Haasteren, S. J. Vigeland, W. Zhu, and NANOGrav Collaboration, The NANOGrav 11-year Data Set: High-precision Timing of 45 Millisecond Pulsars, *Astrophys. J. Suppl. Ser.* **235**, 37 (2018).
- [82] G. Agazie, M. F. Alam, A. Anumarlapudi, A. M. Archibald, Z. Arzoumanian, P. T. Baker, L. Blecha, V. Bonidie, A. Bra-

- zier, P. R. Brook, S. Burke-Spolaor, B. Bécsy, C. Chapman, M. Charisi, S. Chatterjee, T. Cohen, J. M. Cordes, N. J. Cornish, F. Crawford, H. T. Cromartie, K. Crowter, M. E. Deesar, P. B. Demorest, T. Dolch, B. Drachler, E. C. Ferrara, W. Fiore, E. Fonseca, G. E. Freedman, N. Garver-Daniels, P. A. Gentile, J. Glaser, D. C. Good, K. Gültekin, J. S. Hazboun, R. J. Jennings, C. Jessup, A. D. Johnson, M. L. Jones, A. R. Kaiser, D. L. Kaplan, L. Z. Kelley, M. Kerr, J. S. Key, A. Kuske, N. Laal, M. T. Lam, W. G. Lamb, T. J. W. Lazio, N. Lewandowska, Y. Lin, T. Liu, D. R. Lorimer, J. Luo, R. S. Lynch, C.-P. Ma, D. R. Madison, K. Maraccini, A. McEwen, J. W. McKee, M. A. McLaughlin, N. McMann, B. W. Meyers, C. M. F. Mingarelli, A. Mitridate, C. Ng, D. J. Nice, S. K. Ocker, K. D. Olum, E. Panciu, T. T. Pennucci, B. B. P. Perera, N. S. Pol, H. A. Radovan, S. M. Ransom, P. S. Ray, J. D. Romano, L. Salo, S. C. Sardeesai, C. Schmiedekamp, A. Schmiedekamp, K. Schmitz, B. J. Shapiro-Albert, X. Siemens, J. Simon, M. S. Siwek, I. H. Stairs, D. R. Stinebring, K. Stovall, A. Susobhanan, J. K. Swiggum, S. R. Taylor, J. E. Turner, C. Unal, M. Vallisneri, S. J. Vigeland, H. M. Wahl, Q. Wang, C. A. Witt, O. Young, and Nanograv Collaboration, The NANOGrav 15 yr Data Set: Observations and Timing of 68 Millisecond Pulsars, *Astrophys. J. Lett.* **951**, L9 (2023).
- [83] V. Doroshenko, V. Suleimanov, G. Pühlhofer, and A. Santangelo, A strangely light neutron star within a supernova remnant, *Nature Astronomy* **6**, 1444 (2022).
- [84] P. G. Reinhard, The relativistic mean-field description of nuclei and nuclear dynamics, *Reports on Progress in Physics* **52**, 439 (1989).
- [85] M. Bender, P.-H. Heenen, and P.-G. Reinhard, Self-consistent mean-field models for nuclear structure, *Reviews of Modern Physics* **75**, 121 (2003).
- [86] M. G. Alford, L. Brodie, A. Haber, and I. Tews, Relativistic mean-field theories for neutron-star physics based on chiral effective field theory, *Phys. Rev. C* **106**, 055804 (2022).
- [87] Z. Zhu, A. Li, J. Hu, and H. Shen, Equation of state of nuclear matter and neutron stars: Quark mean-field model versus relativistic mean-field model, *Phys. Rev. C* **108**, 025809 (2023).
- [88] Z. Zhu, A. Li, and T. Liu, A Bayesian Inference of a Relativistic Mean-field Model of Neutron Star Matter from Observations of NICER and GW170817/AT2017gfo, *Astrophys. J.* **943**, 163 (2023).
- [89] J. Margueron, R. Hoffmann Casali, and F. Gulminelli, Equation of state for dense nucleonic matter from metamodelling. I. Foundational aspects, *Phys. Rev. C* **97**, 025805 (2018).
- [90] C. Huang, G. Raaijmakers, A. L. Watts, L. Tolos, and C. Providência, Constraining a relativistic mean field model using neutron star mass-radius measurements I: nucleonic models, *Mon. Not. R. Astron. Soc.* **529**, 4650 (2024).
- [91] T. Malik, M. Ferreira, M. B. Albino, and C. Providência, Spanning the full range of neutron star properties within a microscopic description, *Phys. Rev. D* **107**, 103018 (2023).
- [92] M. F. Carney, L. E. Wade, and B. S. Irwin, Comparing two models for measuring the neutron star equation of state from gravitational-wave signals, *Phys. Rev. D* **98**, 063004 (2018).
- [93] D. Wysocki, R. O’Shaughnessy, L. Wade, and J. Lange, Inferring the neutron star equation of state simultaneously with the population of merging neutron stars, *arXiv*, [arXiv:2001.01747](https://arxiv.org/abs/2001.01747) (2020).
- [94] J. S. Read, B. D. Lackey, B. J. Owen, and J. L. Friedman, Constraints on a phenomenologically parameterized neutron-star equation of state, *Phys. Rev. D* **79**, 124032 (2009).
- [95] A. Kedia, H. I. Kim, I.-S. Suh, and G. J. Mathews, Binary neutron star mergers as a probe of quark-hadron crossover equations of state, *Phys. Rev. D* **106**, 103027 (2022).
- [96] I. Legred, Y. Kim, N. Deppe, K. Chatziioannou, F. Foucart, F. Hébert, and L. E. Kidder, Simulating neutron stars with a flexible enthalpy-based equation of state parametrization in SpECTRE, *Phys. Rev. D* **107**, 123017 (2023).
- [97] H. A. Buchdahl, General relativistic fluid spheres, *Phys. Rev.* **116**, 1027 (1959).
- [98] J. M. Lattimer, The Nuclear Equation of State and Neutron Star Masses, *Annu. Rev. Nucl. Part. Sci.* **62**, 485 (2012).
- [99] J. Oppenheimer and G. Volkoff, On Massive neutron cores, *Phys. Rev.* **55**, 374 (1939).
- [100] R. C. Tolman, Static solutions of Einstein’s field equations for spheres of fluid, *Phys. Rev.* **55**, 364 (1939).
- [101] W. Kastaun and F. Ohme, Modern tools for computing neutron star properties, *arXiv e-prints*, [arXiv:2404.11346](https://arxiv.org/abs/2404.11346) (2024).
- [102] W. Kastaun and R. Haas, *wokast/reprimand: Release 1.6* (2024).
- [103] S. K. Greif, G. Raaijmakers, K. Hebeler, A. Schwenk, and A. L. Watts, Equation of state sensitivities when inferring neutron star and dense matter properties, *Mon. Not. R. Astron. Soc.* **485**, 5363 (2019).
- [104] P. Landry, R. Essick, and K. Chatziioannou, Nonparametric constraints on neutron star matter with existing and upcoming gravitational wave and pulsar observations, *Phys. Rev. D* **101**, 123007 (2020).
- [105] J. Alsing, H. O. Silva, and E. Berti, Evidence for a maximum mass cut-off in the neutron star mass distribution and constraints on the equation of state, *Mon. Not. Roy. Astron. Soc.* **478**, 1377 (2018).
- [106] K. Chatziioannou and W. M. Farr, Inferring the maximum and minimum mass of merging neutron stars with gravitational waves, *Phys. Rev. D* **102**, 064063 (2020).
- [107] J. J. Andrews, Mass Ratios of Merging Double Neutron Stars as Implied by the Milky Way Population, *Astrophys. J. Lett.* **900**, L41 (2020).
- [108] M. U. Kruckow, Masses of double neutron star mergers, *Astron. Astrophys.* **639**, A123 (2020).
- [109] N. Farrow, X.-J. Zhu, and E. Thrane, The mass distribution of Galactic double neutron stars, *Astrophys. J.* **876**, 18 (2019).
- [110] A. Vigna-Gómez, C. J. Neijssel, S. Stevenson, J. W. Barrett, K. Belczynski, S. Justham, S. E. de Mink, B. Müller, P. Podsiadlowski, M. Renzo, D. Szécsi, and I. Mandel, On the formation history of Galactic double neutron stars, *Mon. Not. R. Astron. Soc.* **481**, 4009 (2018).
- [111] A. Vigna-Gómez, M. MacLeod, C. J. Neijssel, F. S. Broekgaarden, S. Justham, G. Howitt, S. E. de Mink, S. Vinciguerra, and I. Mandel, Common envelope episodes that lead to double neutron star formation, *Publ. Astron. Soc. Aust.* **37**, e038 (2020).
- [112] V. Kalogera, Spin-Orbit Misalignment in Close Binaries with Two Compact Objects, *Astrophys. J.* **541**, 319 (2000).
- [113] The LIGO Scientific Collaboration, The Virgo Collaboration, The KAGRA Scientific Collaboration, R. Abbott, T. D. Abbott, F. Acernese, K. Ackley, C. Adams, N. Adhikari, R. X. Adhikari, and et al. (LIGO Scientific Collaboration, Virgo Collaboration, and KAGRA Collaboration), The population of merging compact binaries inferred using gravitational waves through GWTC-3, *Phys. Rev. X* **13**, 011048 (2023).
- [114] Y. Y. Yang, C. M. Zhang, D. Li, L. Chen, J. W. Zhang, D. H. Wang, L. Y. Jiang, and X. H. Cui, Investigating the distribution of double neutron stars and unconventional component mass, *Mon. Not. R. Astron. Soc.* **521**, 4669 (2023).
- [115] C. Pankow, On GW170817 and the Galactic Binary Neutron

- Star Population, *Astrophys. J.* **866**, 60 (2018).
- [116] R. D. Ferdman, P. C. C. Freire, B. B. P. Perera, N. Pol, F. Camilo, S. Chatterjee, J. M. Cordes, F. Crawford, J. W. T. Hessels, V. M. Kaspi, M. A. McLaughlin, E. Parent, I. H. Stairs, and J. van Leeuwen, Asymmetric mass ratios for bright double neutron-star mergers, *Nature (London)* **583**, 211 (2020).
- [117] S. Rosswog, P. Diener, F. Torsello, T. M. Tauris, and N. Sarin, Mergers of double NSs with one high-spin component: brighter kilonovae and fallback accretion, weaker gravitational waves, *Mon. Not. R. Astron. Soc.* **530**, 2336 (2024).
- [118] L. J. Papenfort, E. R. Most, S. Tootle, and L. Rezzolla, Impact of extreme spins and mass ratios on the post-merger observables of high-mass binary neutron stars, *Mon. Not. R. Astron. Soc.* **513**, 3646 (2022).
- [119] R. O’Shaughnessy, V. Kalogera, and K. Belczynski, Binary Compact Object Coalescence Rates: The Role of Elliptical Galaxies, *Astrophys. J.* **716**, 615 (2010).
- [120] I. Bartos, S. Rosswog, V. Gayathri, M. C. Miller, D. Veske, and S. Marka, Hierarchical Triples as Early Sources of r -process Elements, *arXiv e-prints*, arXiv:2302.10350 (2023).
- [121] H.-Y. Chen, P. Landry, J. S. Read, and D. M. Siegel, Inference of multi-channel r -process element enrichment in the Milky Way using binary neutron star merger observations, *arXiv e-prints*, arXiv:2402.03696 (2024).
- [122] J. Lange, R. O’Shaughnessy, and M. Rizzo, Rapid and accurate parameter inference for coalescing, precessing compact binaries, *arXiv:1805.10457* (2018).
- [123] The LIGO Scientific Collaboration, the Virgo Collaboration, B. P. Abbott, R. Abbott, T. D. Abbott, and et al, Model comparison from LIGO-Virgo data on GW170817’s binary components and consequences for the merger remnant, *Class. Quantum Grav.* **37**, 045006 (2020).
- [124] E. Fonseca, H. T. Cromartie, T. T. Pennucci, P. S. Ray, A. Y. Kirichenko, S. M. Ransom, P. B. Demorest, I. H. Stairs, Z. Arzoumanian, L. Guillemot, A. Parthasarathy, M. Kerr, I. Cognard, P. T. Baker, H. Blumer, P. R. Brook, M. DeCesar, T. Dolch, F. A. Dong, E. C. Ferrara, W. Fiore, N. Garver-Daniels, D. C. Good, R. Jennings, M. L. Jones, V. M. Kaspi, M. T. Lam, D. R. Lorimer, J. Luo, A. McEwen, J. W. McKee, M. A. McLaughlin, N. McMann, B. W. Meyers, A. Naidu, C. Ng, D. J. Nice, N. Pol, H. A. Radovan, B. Shapiro-Albert, C. M. Tan, S. P. Tendulkar, J. K. Swiggum, H. M. Wahl, and W. W. Zhu, Refined Mass and Geometric Measurements of the High-mass PSR J0740+6620, *Astrophys. J. Lett.* **915**, L12 (2021).
- [125] H. T. Cromartie *et al.*, Relativistic Shapiro delay measurements of an extremely massive millisecond pulsar, *Nature Astron.* **4**, 72 (2019).
- [126] J. Antoniadis, P. C. C. Freire, N. Wex, T. M. Tauris, R. S. Lynch, M. H. van Kerkwijk, M. Kramer, C. Bassa, V. S. Dhillon, T. Driebe, J. W. T. Hessels, V. M. Kaspi, V. I. Kondratiev, N. Langer, T. R. Marsh, M. A. McLaughlin, T. T. Pennucci, S. M. Ransom, I. H. Stairs, J. van Leeuwen, J. P. W. Verbiest, and D. G. Whelan, A Massive Pulsar in a Compact Relativistic Binary, *Science* **340**, 448 (2013).
- [127] P. B. Demorest, T. Pennucci, S. M. Ransom, M. S. E. Roberts, and J. W. T. Hessels, A two-solar-mass neutron star measured using Shapiro delay, *Nature (London)* **467**, 1081 (2010).
- [128] T. Narikawa, N. Uchikata, K. Kawaguchi, K. Kiuchi, K. Kyutoku, M. Shibata, and H. Tagoshi, Reanalysis of the binary neutron star mergers gw170817 and gw190425 using numerical-relativity calibrated waveform models, *Phys. Rev. Res.* **2**, 043039 (2020).
- [129] E. E. Flanagan and T. Hinderer, Constraining neutron star tidal Love numbers with gravitational wave detectors, *Phys. Rev. D* **77**, 021502 (2008).
- [130] T. Dietrich, S. Khan, R. Dudi, S. J. Kapadia, P. Kumar, A. Nagar, F. Ohme, F. Pannarale, A. Samajdar, S. Bernuzzi, G. Carullo, W. Del Pozzo, M. Haney, C. Markakis, M. Pürner, G. Riemenschneider, Y. E. Setyawati, K. W. Tsang, and C. Van Den Broeck, Matter imprints in waveform models for neutron star binaries: Tidal and self-spin effects, *Phys. Rev. D* **99**, 024029 (2019).
- [131] T. Dietrich, A. Samajdar, S. Khan, N. K. Johnson-McDaniel, R. Dudi, and W. Tichy, Improving the NRTidal model for binary neutron star systems, *Phys. Rev. D* **100**, 044003 (2019).
- [132] K. Barkett, Y. Chen, M. A. Scheel, and V. Varma, Gravitational waveforms of binary neutron star inspirals using post-Newtonian tidal splicing, *Phys. Rev. D* **102**, 024031 (2020).
- [133] A. Nagar, S. Bernuzzi, W. Del Pozzo, G. Riemenschneider, S. Akcay, G. Carullo, P. Fleig, S. Babak, K. W. Tsang, M. Colleoni, F. Messina, G. Pratten, D. Radice, P. Rettengo, M. Agathos, E. Fauchon-Jones, M. Hannam, S. Husa, T. Dietrich, P. Cerdá-Duran, J. A. Font, F. Pannarale, P. Schmidt, and T. Damour, Time-domain effective-one-body gravitational waveforms for coalescing compact binaries with nonprecessing spins, tides, and self-spin effects, *Phys. Rev. D* **98**, 104052 (2018).
- [134] B. P. Abbott, R. Abbott, T. D. Abbott, S. Abraham, F. Acernese, K. Ackley, C. Adams, R. X. Adhikari, V. B. Adya, C. Affeldt, and et al., GW190425: Observation of a Compact Binary Coalescence with Total Mass $\sim 3.4 M_{\odot}$, *Astrophys. J. Lett.* **892**, L3 (2020).
- [135] R. Abbott, T. D. Abbott, S. Abraham, F. Acernese, K. Ackley, A. Adams, C. Adams, R. X. Adhikari, V. B. Adya, C. Affeldt, and et al., Observation of Gravitational Waves from Two Neutron Star-Black Hole Coalescences, *Astrophys. J. Lett.* **915**, L5 (2021).
- [136] T. Zhao and J. M. Lattimer, Tidal Deformabilities and Neutron Star Mergers, *Phys. Rev. D* **98**, 063020 (2018).
- [137] M. B. Tsang, J. R. Stone, F. Camera, P. Danielewicz, S. Gandolfi, K. Hebeler, C. J. Horowitz, J. Lee, W. G. Lynch, Z. Kohley, R. Lemmon, P. Möller, T. Murakami, S. Riordan, X. Roca-Maza, F. Sammarruca, A. W. Steiner, I. Vidaña, and S. J. Yenello, Constraints on the symmetry energy and neutron skins from experiments and theory, *Phys. Rev. C* **86**, 015803 (2012).
- [138] B.-A. Li, P. G. Krastev, D.-H. Wen, and N.-B. Zhang, Towards understanding astrophysical effects of nuclear symmetry energy, *European Physical Journal A* **55**, 117 (2019).
- [139] B. D. Metzger, Kilonovae, *Living Reviews in Relativity* **20**, 3 (2017).
- [140] R. Kashyap, A. Das, D. Radice, S. Padamata, A. Prakash, D. Logoteta, A. Perego, D. A. Godzieba, S. Bernuzzi, I. Bombaci, F. J. Fattoyev, B. T. Reed, and A. d. S. Schneider, Numerical relativity simulations of prompt collapse mergers: Threshold mass and phenomenological constraints on neutron star properties after GW170817, *Phys. Rev. D* **105**, 103022 (2022).
- [141] C. Ecker and L. Rezzolla, Impact of large-mass constraints on the properties of neutron stars, *Mon. Not. R. Astron. Soc.* **519**, 2615 (2023).
- [142] D. Choudhury, T. Salmi, S. Vinciguerra, T. E. Riley, Y. Kini, A. L. Watts, B. Dorsman, S. Bogdanov, S. Guillot, P. S. Ray, D. J. Reardon, R. A. Remillard, A. V. Bilous, D. Huppenkothen, J. M. Lattimer, N. Rutherford, Z. Arzoumanian, K. C. Gendreau, S. M. Morsink, and W. C. G. Ho, A NICER View of the Nearest and Brightest Millisecond Pulsar: PSR J0437–4715, *Astrophys. J. Lett.* **971**, L20 (2024).

- [143] I. Mandel, W. M. Farr, and J. R. Gair, Extracting distribution parameters from multiple uncertain observations with selection biases, *Mon. Not. R. Astron. Soc.* **486**, 1086 (2019).
- [144] D. Wysocki, J. Lange, and R. O’Shaughnessy, Reconstructing phenomenological distributions of compact binaries via gravitational wave observations, *Phys. Rev. D* **100**, 043012 (2019).
- [145] W. M. Farr, Accuracy Requirements for Empirically Measured Selection Functions, *Research Notes of the American Astronomical Society* **3**, 66 (2019).
- [146] R. Abbott, T. D. Abbott, S. Abraham, F. Acernese, K. Ackley, C. Adams, R. X. Adhikari, V. B. Adya, C. Affeldt, M. Agathos, and et al., Open data from the first and second observing runs of Advanced LIGO and Advanced Virgo, *SoftwareX* **13**, 100658 (2021).
- [147] The LIGO Scientific Collaboration, The Virgo Collaboration, B. P. Abbott, R. Abbott, T. D. Abbott, F. Acernese, K. Ackley, C. Adams, T. Adams, P. Addesso, and et al., GWTC-1: A Gravitational-Wave Transient Catalog of Compact Binary Mergers Observed by LIGO and Virgo during the First and Second Observing Runs, *Phys. Rev. X* **9**, 031040 (2019).
- [148] L. S. Collaboration, *Parameter estimation sample release for gwtc-1* (2018).
- [149] J. Aasi *et al.* (LIGO Scientific Collaboration), Advanced LIGO, *Class. Quant. Grav.* **32**, 074001 (2015).
- [150] F. Acernese *et al.* (Virgo Collaboration), Advanced Virgo: a second-generation interferometric gravitational wave detector, *Class. Quant. Grav.* **32**, 024001 (2015).
- [151] K. Hotokezaka, E. Nakar, O. Gottlieb, S. Nissanke, K. Masuda, G. Hallinan, K. P. Mooley, and A. T. Deller, A Hubble constant measurement from superluminal motion of the jet in GW170817, *Nat. Astron.* **3**, 940 (2019).
- [152] K. P. Mooley, E. Nakar, K. Hotokezaka, G. Hallinan, A. Corsi, D. A. Frail, A. Hoesli, T. Murphy, E. Lenc, D. L. Kaplan, K. de, D. Dobie, P. Chand ra, A. Deller, O. Gottlieb, M. M. Kasliwal, S. R. Kulkarni, S. T. Myers, S. Nissanke, T. Piran, C. Lynch, V. Bhalerao, S. Bourke, K. W. Bannister, and L. P. Singer, A mildly relativistic wide-angle outflow in the neutron-star merger event GW170817, *Nature (London)* **554**, 207 (2018).
- [153] D. Wysocki, R. O’Shaughnessy, J. Lange, and Y.-L. L. Fang, Accelerating parameter inference with graphics processing units, *Phys. Rev. D* **99**, 084026 (2019).
- [154] J. Wofford, A. B. Yelkar, H. Gallagher, E. Champion, D. Wysocki, V. Delfavero, J. Lange, C. Rose, V. Valsan, S. Morisaki, J. Read, C. Henshaw, and R. O’Shaughnessy, Improving performance for gravitational-wave parameter inference with an efficient and highly-parallelized algorithm, *Phys. Rev. D* **107**, 024040 (2023).
- [155] J. A. J. Alford and J. P. Halpern, Do Central Compact Objects have Carbon Atmospheres?, *Astrophys. J.* **944**, 36 (2023).
- [156] V. Sagun, E. Giangrandi, T. Dietrich, O. Ivanytskyi, R. Negreiros, and C. Providência, What Is the Nature of the HESS J1731-347 Compact Object?, *Astrophys. J.* **958**, 49 (2023).
- [157] J. J. Li and A. Sedrakian, Baryonic models of ultra-low-mass compact stars for the central compact object in HESS J1731-347, *Physics Letters B* **844**, 138062 (2023).
- [158] L. Brodie and A. Haber, Nuclear and hybrid equations of state in light of the low-mass compact star in HESS J1731-347, *Phys. Rev. C* **108**, 025806 (2023).
- [159] J. E. Horvath, L. S. Rocha, L. M. de Sá, P. H. R. S. Moraes, L. G. Barão, M. G. B. de Avellar, A. Bernardo, and R. R. A. Bachega, A light strange star in the remnant HESS J1731–347: Minimal consistency checks, *Astron. Astrophys.* **672**, L11 (2023).
- [160] J.-L. Jiang, C. Ecker, and L. Rezzolla, Bayesian Analysis of Neutron-star Properties with Parameterized Equations of State: The Role of the Likelihood Functions, *Astrophys. J.* **949**, 11 (2023).
- [161] P. Laskos-Patkos, P. S. Koliogiannis, and C. C. Moustakidis, Hybrid stars in light of the hess j1731-347 remnant and the pre-xii experiment, *Phys. Rev. D* **109**, 063017 (2024).
- [162] S. Shirke, S. Ghosh, and D. Chatterjee, Constraining the Equation of State of Hybrid Stars Using Recent Information from Multidisciplinary Physics, *Astrophys. J.* **944**, 7 (2023).
- [163] S. Vinciguerra, T. Salmi, A. L. Watts, D. Choudhury, T. E. Riley, P. S. Ray, S. Bogdanov, Y. Kini, S. Guillot, D. Chakrabarty, W. C. G. Ho, D. Huppenkothen, S. M. Morsink, Z. Wadiasingh, and M. T. Wolff, An Updated Mass-Radius Analysis of the 2017-2018 NICER Data Set of PSR J0030+0451, *Astrophys. J.* **961**, 62 (2024).
- [164] A. Kurkela, P. Romatschke, and A. Vuorinen, Cold quark matter, *Phys. Rev. D* **81**, 105021 (2010).
- [165] E. Annala, T. Gorda, A. Kurkela, J. Nättilä, and A. Vuorinen, Evidence for quark-matter cores in massive neutron stars, *Nature Physics* **16**, 907 (2020).
- [166] K. Wagner, R. O’Shaughnessy, and et al, RIFT documentation, <https://rift-documentation.readthedocs.io/en/latest/> (2024).
- [167] T. E. Riley, A. L. Watts, S. Bogdanov, P. S. Ray, R. M. Ludlam, S. Guillot, Z. Arzoumanian, C. L. Baker, A. V. Bilous, D. Chakrabarty, K. C. Gendreau, A. K. Harding, W. C. G. Ho, J. M. Lattimer, S. M. Morsink, and T. E. Strohmayer, A NICER View of PSR J0030+0451: Nested Samples for Millisecond Pulsar Parameter Estimation, [10.5281/zenodo.3386449](https://doi.org/10.5281/zenodo.3386449) (2019).
- [168] M. C. Miller, F. K. Lamb, A. J. Dittmann, S. Bogdanov, Z. Arzoumanian, K. C. Gendreau, S. Guillot, A. K. Harding, W. C. G. Ho, J. M. Lattimer, R. M. Ludlam, S. Mahmoodifar, S. M. Morsink, P. S. Ray, T. E. Strohmayer, K. S. Wood, T. Enoto, R. Foster, T. Okajima, G. Prigozhin, and Y. Soong, NICER PSR J0030+0451 Illinois-Maryland MCMC Samples, [10.5281/zenodo.3473466](https://doi.org/10.5281/zenodo.3473466) (2019).
- [169] T. E. Riley, A. L. Watts, P. S. Ray, S. Bogdanov, S. Guillot, S. M. Morsink, A. V. Bilous, Z. Arzoumanian, D. Choudhury, J. S. Deneva, K. C. Gendreau, A. K. Harding, W. C. Ho, J. M. Lattimer, M. Loewenstein, R. M. Ludlam, C. B. Markwardt, T. Okajima, C. Prescod-Weinstein, R. A. Remillard, M. T. Wolff, E. Fonseca, H. T. Cromartie, M. Kerr, T. T. Pennucci, A. Parthasarathy, S. Ransom, I. Stairs, L. Guillemot, and I. Cognard, A NICER View of the Massive Pulsar PSR J0740+6620 Informed by Radio Timing and XMM-Newton Spectroscopy: Nested Samples for Millisecond Pulsar Parameter Estimation, [10.5281/zenodo.4697625](https://doi.org/10.5281/zenodo.4697625) (2021).
- [170] M. Miller, F. K. Lamb, A. J. Dittmann, S. Bogdanov, Z. Arzoumanian, K. C. Gendreau, S. Guillot, W. C. G. Ho, J. M. Lattimer, S. M. Morsink, P. S. Ray, M. T. Wolff, C. L. Baker, T. Cazeau, S. Manthripragada, C. B. Markwardt, T. Okajima, S. Pollard, I. Cognard, H. T. Cromartie, E. Fonseca, L. Guillemot, M. Kerr, A. Parthasarathy, T. T. Pennucci, S. Ransom, I. Stairs, and M. Loewenstein, NICER PSR J0740+6620 Illinois-Maryland MCMC Samples, [10.5281/zenodo.4670689](https://doi.org/10.5281/zenodo.4670689) (2021).
- [171] B. D. Lackey and L. Wade, Reconstructing the neutron-star equation of state with gravitational-wave detectors from a realistic population of inspiralling binary neutron stars, *Phys. Rev. D* **91**, 043002 (2015).
- [172] R. Huxford, R. Kashyap, S. Borhanian, A. Dhani, and B. S. Sathyaprakash, The Accuracy of Neutron Star Ra-

- dus Measurement with the Next Generation of Terrestrial Gravitational-Wave Observatories, [arXiv e-prints](#), [arXiv:2307.05376](#) (2023).
- [173] A. Bandopadhyay, K. Kacanja, R. Somasundaram, A. H. Nitz, and D. A. Brown, Measuring neutron star radius with second and third generation gravitational wave detector networks, [Class. Quantum Grav.](#) **41**, 225003 (2024).
- [174] D. Finstad, L. V. White, and D. A. Brown, Prospects for a Precise Equation of State Measurement from Advanced LIGO and Cosmic Explorer, [Astrophys. J.](#) **955**, 45 (2023).
- [175] L. S. Finn and D. F. Chernoff, Observing binary inspiral in gravitational radiation: One interferometer, [Phys. Rev. D](#) **47**, 2198 (1993).
- [176] C. Cutler and É. E. Flanagan, Gravitational waves from merging compact binaries: How accurately can one extract the binary's parameters from the inspiral waveform?, [Phys. Rev. D](#) **49**, 2658 (1994).
- [177] R. O'Shaughnessy, B. Vaishnav, J. Healy, and D. Shoemaker, Intrinsic selection biases of ground-based gravitational wave searches for high-mass black hole-black hole mergers, [Phys. Rev. D](#) **82**, 104006 (2010).
- [178] H. Rose, N. Kunert, T. Dietrich, P. T. H. Pang, R. Smith, C. Van Den Broeck, S. Gandolfi, and I. Tews, Revealing the strength of three-nucleon interactions with the proposed Einstein Telescope, [Phys. Rev. C](#) **108**, 025811 (2023).
- [179] K. Walker, R. Smith, E. Thrane, and D. J. Reardon, Precision constraints on the neutron star equation of state with third-generation gravitational-wave observatories, [Phys. Rev. D](#) **110**, 043013 (2024).
- [180] A. Zic, D. J. Reardon, A. Kapur, G. Hobbs, R. Mandow, M. Curyło, R. M. Shannon, J. Askew, M. Bailes, N. D. R. Bhat, A. Cameron, Z.-C. Chen, S. Dai, V. Di Marco, Y. Feng, M. Kerr, A. Kulkarni, M. E. Lower, R. Luo, R. N. Manchester, M. T. Miles, R. S. Nathan, S. Osłowski, A. F. Rogers, C. J. Russell, J. M. Sarkissian, M. Shamohammadi, R. Spiewak, N. Thyagarajan, L. Toomey, S. Wang, L. Zhang, S. Zhang, and X.-J. Zhu, The Parkes Pulsar Timing Array third data release, [Publ. Astron. Soc. Aust.](#) **40**, e049 (2023).